

The convection connection: how ocean feedbacks affect tropical mean moisture and MJO propagation

Article

Accepted Version

Demott, C. A., Klingaman, N., Tseng, W.-L., Burt, M. A., Gao, Y. and Randall, D. A. (2019) The convection connection: how ocean feedbacks affect tropical mean moisture and MJO propagation. *Journal of Geophysical Research*, 124 (22). pp. 11910-11931. ISSN 0148-0227 doi: <https://doi.org/10.1029/2019JD031015> Available at <https://centaur.reading.ac.uk/86867/>

It is advisable to refer to the publisher's version if you intend to cite from the work. See [Guidance on citing](#).

To link to this article DOI: <http://dx.doi.org/10.1029/2019JD031015>

Publisher: American Geophysical Union

All outputs in CentAUR are protected by Intellectual Property Rights law, including copyright law. Copyright and IPR is retained by the creators or other copyright holders. Terms and conditions for use of this material are defined in the [End User Agreement](#).

www.reading.ac.uk/centaur

CentAUR

Central Archive at the University of Reading

Reading's research outputs online

The convection connection: How ocean feedbacks affect tropical mean moisture and MJO propagation

Charlotte A. DeMott¹, Nicholas P. Klingaman², Wan-Ling Tseng³, Melissa A. Burt¹, Yingxia Gao⁴, and David A. Randall¹

¹Department of Atmospheric Science, Colorado State University, Fort Collins Colorado USA

²National Centre for Atmospheric Science, University of Reading, Reading UK

³Research Center for Environmental Changes, Academia Sinica, Taipei, Taiwan

⁴International Laboratory on Climate and Environment Change and Key Laboratory of Meteorological Disaster of Ministry of Education, Nanjing University of Information Science and Technology, Nanjing, China

Key Points:

- Coupled and uncoupled simulations with identical SST climatology yield non-identical MJOs in four GCMs
- For all models, coupling enhances mean meridional moisture gradients and improves MJO propagation via meridional moisture advection
- Coupling enhances convective moistening at high rainrates and sharpens the moisture gradients

Corresponding author: Charlotte A. DeMott, Charlotte.DeMott@ColoState.edu

Abstract

The response of the Madden-Julian oscillation (MJO) to ocean feedbacks is studied with coupled and uncoupled simulations of four general circulation models (GCMs). Monthly mean SST from each coupled model is prescribed to its respective uncoupled simulation, to ensure identical SST mean state and low-frequency variability between simulation pairs. Consistent with previous studies, coupling improves each model’s ability to propagate MJO convection beyond the Maritime Continent. Analysis of the MJO moist static energy budget reveals that improved MJO eastward propagation in all four coupled models arises from enhanced meridional advection of column water vapor (CWV). Despite the identical mean state SST in each coupled and uncoupled simulation pair, coupling increases mean-state CWV near the Equator, sharpening equatorward moisture gradients and enhancing meridional moisture advection and MJO propagation. CWV composites during MJO and non-MJO periods demonstrate that the MJO itself does not cause enhanced moisture gradients. Instead, analysis of low-level subgrid-scale moistening conditioned by rainfall rate (R) and SST anomaly reveals that coupling enhances low-level convective moistening for $R > 5 \text{ mm day}^{-1}$; this enhancement is most prominent near the Equator. The low-level moistening process varies among the four models, which we interpret in terms of their ocean model configurations, cumulus parameterizations, and sensitivities of convection to column relative humidity.

1 Introduction

The importance of ocean feedbacks to the Madden-Julian oscillation (MJO; Madden & Julian, 1972) has been a focus of inquiry for decades (DeMott et al., 2015). While consensus thinking holds that the MJO is primarily an atmospheric phenomenon, its sensitivity to SST-driven surface flux feedbacks is supported by observational (Riley Delaripa & Maloney, 2015; DeMott et al., 2016), theoretical (B. Wang & Xie, 1998), and modeling studies (e.g., Zhang & McPhaden, 2000; Seo et al., 2007; Klingaman & Woolnough, 2014, and others). Understanding how, and the degree to which, these feedbacks influence MJO intensity or propagation is fraught with challenges. For example, the observed MJO always develops in a coupled environment, yet the nature of ocean feedbacks to the MJO vary from one event to the next (Gottschalck et al., 2013; Fu et al., 2015; Moum et al., 2016). In models, coupling changes MJO surface fluxes, which initiates changes to the entire MJO, affecting the balance of atmospheric processes that dominate MJO

50 maintenance and propagation (e.g., DeMott et al., 2014; Klingaman & Woolnough, 2014).
 51 SST-driven surface fluxes may affect the MJO through any of a variety of processes that
 52 influence both the background state and the intraseasonal convection throughout the MJO
 53 lifecycle. Modeling studies focused on understanding the role of coupling within the MJO
 54 are hampered by different mean-state biases in coupled and uncoupled simulations that
 55 themselves affect the MJO (Slingo & co authors, 1996; Sperber et al., 2005; Zhang et al.,
 56 2006; Klingaman & Woolnough, 2014) and complicate the interpretation of ocean feed-
 57 backs.

58 One way to minimize complications from mean-state differences between coupled
 59 and atmosphere-only general circulation models (CGCMs and AGCMs, respectively) is
 60 to prescribe temporally smoothed SSTs from the CGCM to the AGCM. While this ap-
 61 proach allows a cleaner comparison of intraseasonal variability in CGCM and AGCM
 62 simulations, CGCM mean-state SST biases present in both the coupled and uncoupled
 63 simulations may affect MJO propagation in a manner different than observed. CGCM
 64 mean-state biases can be mitigated by replacing the three-dimensional (3D) dynamical
 65 ocean in the CGCM with either a single-layer “slab” ocean (Waliser et al., 1999; Wat-
 66 terson, 2002; Maloney & Sobel, 2004; Marshall et al., 2008; Benedict & Randall, 2011)
 67 or a multi-layer, one-dimensional (1D) ocean mixed-layer (Klingaman & Woolnough, 2014;
 68 Tseng et al., 2015). With these approaches, SST can respond to atmospheric forcing, but
 69 mean SST is constrained to the observed climatology via surface-flux adjustments (for
 70 the slab ocean) or seasonally varying salt and heat advection (for the mixed layer). How-
 71 ever, slab- and mixed layer-coupled GCMs exclude ocean dynamic feedbacks that may
 72 influence intraseasonal SST perturbations (Harrison & Vecchi, 2001; Saji et al., 2006; McPhaden
 73 & Foltz, 2013; Seiki et al., 2013; Moum et al., 2013; Halkides et al., 2015).

74 Many experiments with CGCMs and AGCMs with the same SST climatology have
 75 demonstrated that coupling improves several aspects of the simulated MJO, including
 76 its amplitude, periodicity, propagation, and prediction (see DeMott et al. (2015), Sec-
 77 tion 5 for a full review). Improved phasing of SST, surface fluxes, and MJO convection
 78 are often cited as reasons for these improvements (e.g., Marshall et al., 2008; Pegion &
 79 Kirtman, 2008), but changes to MJO circulation (Zhang et al., 2006), including stronger
 80 free tropospheric wind anomalies (Watterson, 2002; DeMott et al., 2014), and enhanced
 81 boundary-layer frictional convergence ahead of MJO convection (Kemball-Cook et al.,
 82 2002; Benedict & Randall, 2011; Fu et al., 2015) have also been noted.

Many of these CGCM-AGCM studies predate important advances in understanding and diagnosing the processes that regulate MJO activity. For example, the moist static energy (MSE) budget (Maloney, 2009; Andersen & Kuang, 2012) provides a framework to assess processes that contribute to MJO maintenance and propagation, including the relative roles of intraseasonal SST variations on MJO surface fluxes (Maloney & Sobel, 2004; DeMott et al., 2016); the effects of suppressed-phase conditions on subsequent MJO propagation (Kim et al., 2014); the importance of cloud–radiative feedbacks for destabilizing and maintaining MJO convection (Andersen & Kuang, 2012; Arnold & Randall, 2015); the role of background moisture gradients on MJO moistening tendencies (Kim et al., 2017; Gonzalez & Jiang, 2017; DeMott et al., 2018); and SST-driven amplification of boundary-layer frictional convergence east of MJO convection (W. Wang & Seo, 2009; Benedict & Randall, 2011; Hsu & Li, 2012; L. Wang et al., 2017).

We revisit the role of ocean coupling for the MJO using CGCM and AGCM simulations of four GCMs. Mean state differences between each pair of simulations are reduced by prescribing monthly mean or 31-day running mean SST from the CGCM (rather than observed SSTs) to the AGCM.. We seek to determine if the models share a fundamental ocean feedback that improves MJO simulation, or if each model relies upon its own unique coupled feedback mechanism to improve its MJO simulation. Our paper is organized as follows: Models and reanalysis products are described in Section 2. MJO skill metrics and MSE budgets analyses are summarized in Section 3. In Section 4, we compare mean CWV during MJO and non-MJO periods to determine the effect of the MJO on the meridional CWV distribution in CGCMs. In Section 5, we propose that the CWV changes with coupling can be understood by considering convective moistening conditioned by rainfall rate and SSTA. In Section 6, we discuss how each model’s particular combination of cumulus parameterization and ocean vertical resolution may lead to moistening characteristics that favor MJO propagation. A summary and suggestions for future research are provided in Section 7.

2 Methods

Here, we describe the models used in this study, and introduce the moist static energy (MSE) and moisture budgets. Metrics to quantify MJO simulation fidelity (i.e., its accuracy or realism), structure, and circulations are described in Section 3.2.

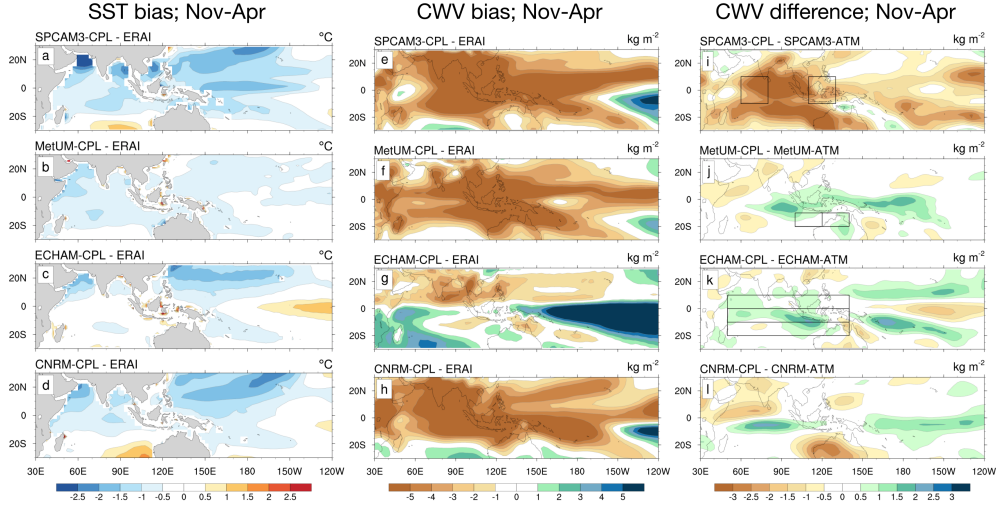


Figure 1. November–April mean state SST (a–d) and CWV (e–h) biases, and coupled–
 uncoupled mean state CWV differences (i–l) for the four models analyzed. Overlaid boxes are
 averaging regions used to compute i) zonal, j) MJO “detour” region and k) meridional CWV
 differences (Section 3.2)

2.1 Models and Data

The four models used in this study are: the Super-Parameterized Community Atmospheric Model (version 3) (SPCAM3; Khairoutdinov et al., 2005), the Global Ocean Mixed Layer configuration of Met Office Unified Model (MetUM; Walters et al., 2011; Hirons et al., 2015)), the Max Planck Institute’s European Centre-Hamburg (ECHAM, v6; Stevens et al., 2013), and the Centre National de Recherches Météorologiques (CNRM; Voldoire et al., 2012). SPCAM3 and CNRM are coupled to a 3D ocean model while MetUM and ECHAM are coupled to many columns of a 1D ocean mixed-layer model. For the latter, oceanic salt and heat tendency profiles are prescribed to minimize mean-state SST biases (see Hirons et al. (2015) for details for MetUM). The one-column ocean model in ECHAM5-CPL describes changes in temperature, momentum, salinity, and turbulent kinetic energy driven by vertical fluxes parameterized using the classical K approach [Tseng et. al., 2015]. No such corrections are applied to coupled simulations with SPCAM3 and CNRM. November–April mean SST biases for each model are shown in the left column of Figure 1. In an area-averaged sense, magnitudes of the CWV biases generally reflect the magnitudes of the SST biases (middle column of Figure 1). The right column of Figure 1 is discussed in Section 3.2.

146

Table 1. Atmospheric and oceanic model descriptions and resolution.

Coupled, uncoupled simulation	Atmosphere	Ocean (for coupled)
SPCAM3-CPL SPCAM3-ATM	Super-Parameterized Community Atmospheric Model (v3); $\approx 2.5^\circ \times 1.8^\circ$ (Khairoutdinov et al., 2005; Stan et al., 2010)	3D Parallel Ocean Program version 1.4.3; $\approx 3^\circ$ resolution near Equator (POP; Smith & Gent, 2002)
MetUM-CPL MetUM-ATM	UK Met Office Unified Model; $\approx 1.9^\circ \times 1.25^\circ$ (GA3; Walters et al., 2011)	1D Global K Profile Parameterization ocean mixed layer; same resolution as atmosphere (Large et al., 1994; Hirons et al., 2015)
ECHAM-CPL ECHAM-ATM	ECHAM (v5); $\approx 1.8^\circ \times 1.8^\circ$ (Stevens et al., 2013)	1D Snow-Ice-Thermocline (SIT); same resolution as atmosphere (Tseng et al., 2015)
CNRM-CPL CNRM-ATM	CNRM (v5.2); $\approx 1.4^\circ \times 1.4^\circ$ (Voldoire et al., 2012)	3D NEMO; $\approx 1^\circ$ resolution near Equator (Madec, 2008)

Each CGCM is integrated for 20–25 years. Monthly mean (SPCAM3 and CNRM) or 31-day running mean (MetUM and ECHAM) SST time series from each CGCM are prescribed to its respective AGCM. This ensures that the CGCM and AGCM have identical SST mean state and low-frequency variability; only SST variability on frequencies higher than 31 days is absent in the AGCMs. Removal of high-frequency SST variability from the AGCM may affect our results, but including this variability by prescribing daily mean SST to the AGCM, for example, is known to unrealistically alter the phasing of rainfall and SST (e.g., Pegion & Kirtman, 2008; DeMott et al., 2015). The four CGCMs are denoted as SPCAM3-CPL, MetUM-CPL, ECHAM-CPL, and CNRM-CPL, while their AGCM counterparts are SPCAM3-ATM, MetUM-ATM, ECHAM-ATM, and CNRM-ATM, respectively. Model descriptions and references are summarized in Table 1.

Results from all simulations are compared to daily mean data from the European Centre for Medium Range Forecasts (ECWMF) Interim Reanalysis (ERA-Interim; Dee & co authors, 2011) on a $2.5^\circ \times 2.5^\circ$ grid for 1986–2013 (Dee & co authors, 2011).

2.2 Analysis Methods

Processes responsible for the maintenance and propagation of MJO convection are assessed with the aid of the moist static energy (MSE) budget:

$$\partial \langle m \rangle / \partial t = -\langle V \cdot \nabla m \rangle - \langle \omega \partial m / \partial p \rangle + \langle LW \rangle + \langle SW \rangle + LH + SH \quad (1)$$

where m is the MSE, defined as $m = C_p T + L_v q + gz$ [J kg^{-1}], T is temperature [K], q is specific humidity [kg kg^{-1}], z is height [m], V is the horizontal wind [m s^{-1}], ω is the vertical pressure velocity [Pa s^{-1}], LH and SH are surface latent and sensible heat fluxes [W m^{-2}], respectively, and LW and SW are longwave and shortwave radiative heating [K s^{-1}]. Angled brackets denote integration from the surface to 100 mb, yielding units of [W m^{-2}] for all terms. From left to right, terms on the right hand side of Equation 1 are MSE horizontal and vertical advection, column-integrated longwave and shortwave radiative heating, and surface latent and sensible heat fluxes.

In the Tropics, MSE tendencies are largely driven by moisture tendencies, as the weak Coriolis force enables rapid dissipation of temperature and density anomalies via gravity waves. Compared to moisture budgets, MSE budgets are useful for understanding tropical convective variability because rainfall and MSE are highly correlated, MSE is conserved during diabatic phase changes (eliminating the need to accurately observe rainfall), and the column MSE budget includes radiative and surface sensible heat fluxes. MSE budget analysis is a standard tool to assess processes responsible for MJO maintenance and propagation (e.g., Maloney, 2009; Andersen & Kuang, 2012).

Each term in Equation 1 is computed using daily mean input variables; its anomaly is computed as the difference between the daily mean value and the slowly varying “background” state, which is obtained by applying a low-pass filter with a 100 day cutoff to the daily mean time series. This partitions subseasonal and higher-frequency variability into the anomaly time series, and seasonal and lower-frequency variability into the background-state time series. SST and other state variables are partitioned the same way. Intraseasonal rainfall anomalies are obtained with a 20-100 day 201 point Lanczos filter.

We also computed daily mean, vertically resolved moisture budget terms and the moisture budget residual, which is the apparent moisture sink (Q_2 ; Yanai et al., 1973):

$$Q_2/L_v = -[\partial q/\partial t + \nabla \cdot (qV) + \partial(q\omega)/\partial p] = (c - e) + \partial(q'w')/\partial p \quad (2)$$

where q is the specific humidity, c and e are the condensation and evaporation of water vapor, respectively, and $\partial(q'w')/\partial p$ is the unresolved vertical eddy flux of water vapor. When written as $-Q_2/L_v$ [$\text{kg kg}^{-1} \text{s}^{-1}$], positive values of the budget residual represent unresolved moistening by convection (Section 5). For ERAI, $-Q_2/L_v$ also includes moistening from data assimilation increments.

3 MJO simulation assessment

3.1 MJO propagation and MSE budget overview

MJO propagation in ERAI and the eight simulations is illustrated with rainfall lagged-regression plots (Figure 2). ERAI and the coupled simulations (left column) show coherent propagation across the Indian Ocean and Maritime Continent. Robust propagation continues to about 165°E in ERAI, SPCAM3-CPL, and CNRM-CPL, while weaker propagation is observed in MetUM-CPL and ECHAM-CPL. The 20–100 day rainfall standard deviation (R) for each CGCM is larger than that in ERAI. Some of this difference may be a reflection of suspected “missing” rainfall processes in ERAI, as indicated by less frequent heavy rainfall rates compared to satellite-derived rainfall products (e.g., Adames et al., 2017). R in AGCMs (right column) is reduced in all models but ECHAM-ATM, an indication that improved MJO fidelity with coupling is not uniformly linked to enhanced intraseasonal heating variability. AGCMs produce westward-propagating (SPCAM3-ATM), stationary (MetUM-ATM), or weakly eastward-propagating (ECHAM-ATM, CNRM-ATM) disturbances. MJO propagation fidelity is assessed using a method adapted from Jiang et al. (2015): the MJO “pattern correlation” metric, r , is the correlation between the rainfall lagged-regression diagram for each model (Figures 2b–i) with the ERAI lagged-regression diagram (Figure 2a). Correlations are computed for regressions against 90°E and 150°E basepoints (not shown) and averaged. Rainfall within $\pm 15^\circ$ longitude of each basepoint is omitted since it unfavorably weights the result by MJO periodicity, rather than by MJO propagation (c.f., L. Wang et al., 2017).

Figure 3 presents CGCM MSE component contributions (Equation 1) to MSE maintenance (Figure 3a) and tendency (Figure 3b) integrated over the MJO lifecycle and the

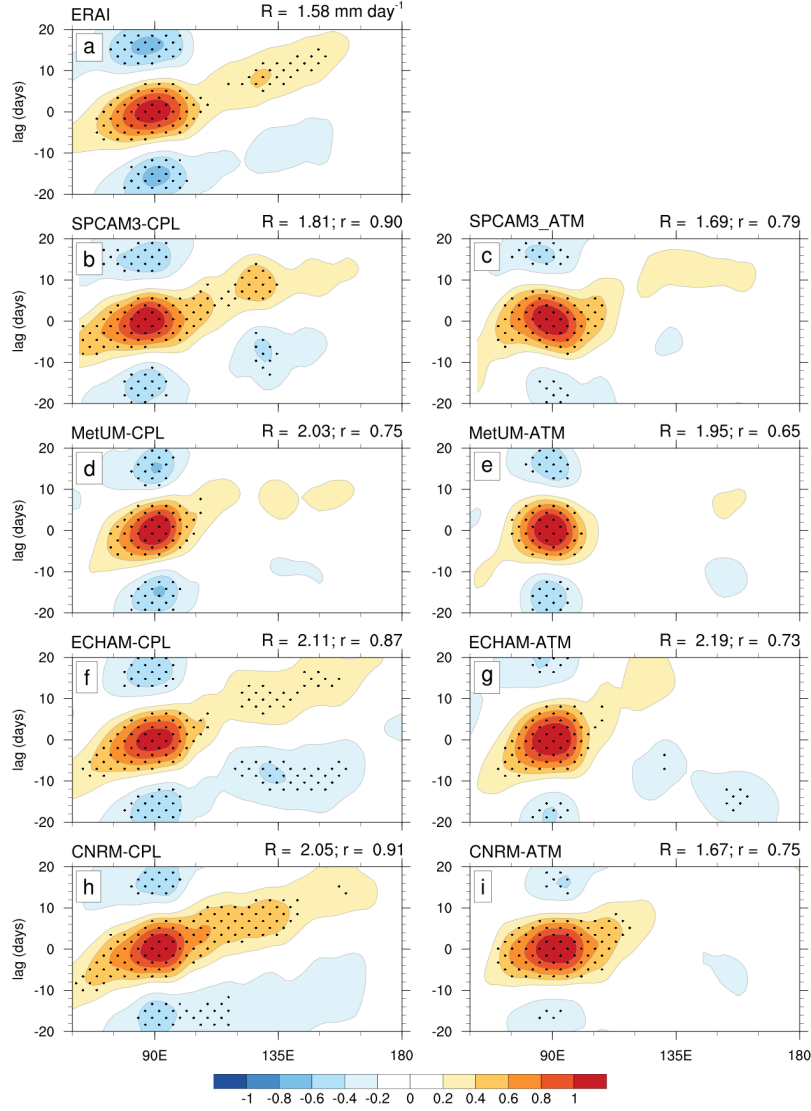


Figure 2. Lag-regression of November–April 15°S–15°N averaged rainfall anomalies onto 20–100 day filtered rainfall at a 90°E basepoint (80°E–100°E and 15°S–15°N area average). Coupled (uncoupled) systems are plotted in the left (right) column. 20–100 day basepoint rainfall standard deviation (R), and the average pattern correlation for 90°E and 150°E basepoints (r ; see text for details) are listed on each panel. Units for R and contoured values are mm day^{-1} . Stippling denotes significance at the 95% confidence interval.

Warm Pool. Following DeMott et al. (2016), these contributions were computed by regressing individual MSE component anomalies onto November–April 20–100 day filtered MSE and its tendency, respectively, at each grid point. Regression coefficients are averaged from 15°S to 15°N and 30°E to 240°E to include the Warm Pool and regions farther east affected by MJO circulation anomalies (results are similar for a 180°E eastern boundary). Figure 3 combines $\langle LW \rangle$ and $\langle SW \rangle$ and LH and SH ; the second term in each pair is an order of magnitude smaller than the first. Consistent with many previous studies (Andersen & Kuang, 2012; Kiranmayi & Maloney, 2011; DeMott et al., 2016), MSE anomalies are principally maintained by $\langle LW \rangle$. MSE vertical advection ($\langle -\omega \frac{\partial m}{\partial p} \rangle$; VADV) and surface fluxes are both MSE sinks (SPCAM3-CPL is an exception, where vertical advection is small source term). The MSE tendency, which maximizes to the east of MJO convection, and contributes to its eastward propagation, is dominated by horizontal MSE advection ($\langle -V \cdot \nabla m \rangle$; HADV), with minor contributions from $\langle -\omega \frac{\partial m}{\partial p} \rangle$. From this area- and lifecycle-averaged perspective, surface fluxes do not significantly contribute to MJO maintenance or propagation.

This raises an important question: How can ocean feedbacks—which are communicated to the atmosphere through SST-modulated surface fluxes—so distinctly improve the fidelity of the simulated MJO? DeMott et al. (2016) analyzed the spatial structure of SST-modulated surface flux contributions to the MJO with ERAI data and found that direct ocean feedbacks account for up to 1–2% of MSE maintenance near the Equator and $\approx 10\%$ of MSE tendency across the Warm Pool. We obtained similar results for the CGCMs (not shown). Based on these findings, it seems unlikely that direct ocean feedbacks to MJO convection or its tendency can explain the improved MJO propagation in the coupled simulations. Instead, coupled surface fluxes most likely affect MJO propagation through more indirect feedbacks, such as altering the atmospheric stability profile to strengthen the circulation response to MJO heating, or by changing mean state conditions.

3.2 MJO and process metrics

To better understand how coupling affects the MJO, we computed a variety of metrics of MJO propagation, period, circulation structure, and mean state, and compared how these metrics change with coupling. Here, we define each metric and its shorthand name, which is later referenced in Figure 5. MJO propagation is assessed with the afore-

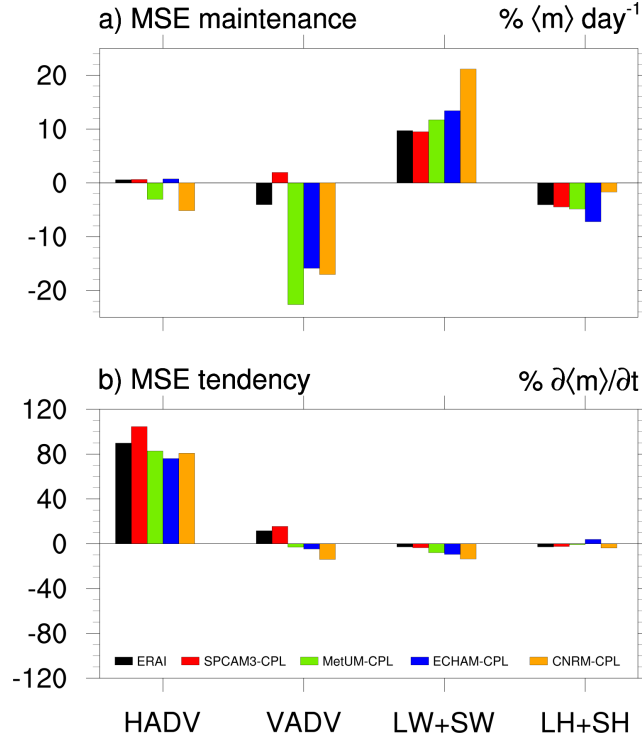


Figure 3. November–April area-averaged (15°S – 15°N ; 30°E – 240°E) covariability of MSE budget terms (Equation 1) with 20–100 day filtered a) $\langle m \rangle$ and b) $\langle \frac{\partial m}{\partial t} \rangle$.

mentioned pattern correlation (“Pattern Corr.”). Another measure of MJO propagation is the east-west power ratio which is the ratio of rainfall variance for eastward- and westward-propagating zonal wave numbers 1–3 and periods 30–60 days (“EW ratio;” Jiang et al., 2015). MJO period is defined as twice the number of days between the maximum and minimum lagged auto-correlation of 20–100 day filtered 90°E rainfall (“Period”).

MJO circulation metrics are computed with the aid of maps of anomalous 850 hPa zonal winds (Figure 4a–e), $\langle LW \rangle$ (Figure 4f–j), and 850 hPa vertical moisture advection (Figure 4k–o) regressed onto 20–100 day band pass filtered 90°E rainfall. MJO-associated zonal wind anomalies show an elongated region of low-level easterlies to the east, and a more truncated region of low-level westerlies to the west. The low-level easterlies arise from the Kelvin-wave response to Indian Ocean convective heating (Gill, 1980) and the equatorial Rossby-wave response to Maritime Continent and West Pacific longwave cooling (Kim et al., 2012). The low-level westerlies are part of the equatorially symmetric Rossby wave response to positive Indian Ocean heating. The magnitudes of the Kelvin-wave easterlies (“KW wind”) and Rossby-wave westerlies (“ER wind”) are the maximum

5°N to 5°S averaged easterly and westerly wind anomalies. Their ratio (“KW/ER ratio”) is positively correlated with MJO propagation fidelity (B. Wang et al., 2018). A “dry phase intensity” index, defined as anomalous longwave cooling < -1 [W m⁻²]/[mm day⁻¹] integrated from 20°S–20°N and 100°E–210°E (the “Dry Phase” metric), measures the strength of longwave cooling that initiates poleward flow east of MJO convection as part of the anticyclonic Rossby gyre response to the negative heating anomaly (Kim et al., 2012). 850 hPa vertical moisture advection, $-\omega \frac{\partial q}{\partial p}|_{850}$, averaged over 5°S–5°N and 110°E–180°E (the “BL export” metric) measures low-level convergence-driven export of moisture from the boundary layer to the free troposphere, which may be critical to MJO propagation (e.g., Hsu & Li, 2012; B. Wang et al., 2018).

MJO propagation is critically sensitive to mean-state moisture gradients, which regulate horizontal moisture advection by MJO wind anomalies (Kim et al., 2012, 2017; Gonzalez & Jiang, 2017; Lim et al., 2018; DeMott et al., 2018). November–April mean CWV for ERAI and CGCMs and the averaging regions used to compute moisture gradient metrics are shown in Figure 1i–k. The Warm Pool zonal moisture gradient (“dCWV/dx (WP)”) is the difference between CWV averaged over the Maritime Continent (10°S–10°N; 110°E–130°E) and the central Indian Ocean (10°S–10°N; 60°E–80°E). We also compute the zonal moisture gradient in the MJO “detour” region (Kim et al., 2017) as the difference between area-averaged CWV north of Australia (20°S–10°S; 120°E–135°E) and south of Sumatra (20°S–10°S; 105°E–120°E (the “dCWV/dx (Aus)” metric). Northern (“dCWV/dy (nIO)”) and southern (“dCWV/dy (sIO)”) meridional moisture gradients are computed as the area-averaged CWV difference between the November–April “moisture Equator” (10°S–0°N; 40°E–120°E) and (0°N–10°N; 40°E–120°E) and (20°S–10°S; 40°E–120°E), respectively. Northern and southern gradients are averaged to yield the mean equatorward moisture gradient (“dCWV/dy (IO)”).

3.3 Changes to MJO metrics with coupling

The effects of coupled feedbacks on the above MJO metrics and MSE budget term contributions to MJO maintenance and propagation are summarized in Figure 5. Changes to metrics that characterize MJO propagation, circulation, intensity, and period are plotted in Figure 5a as the coupled minus uncoupled percentage difference (i.e., $\Delta M = 100 \cdot (M_{CPL} - M_{ATM}) / M_{ATM}$ where subscripts “CPL” and “ATM” refer to CGCM and AGCM metrics, respectively). As previously noted, coupling does not uniformly increase intrasea-

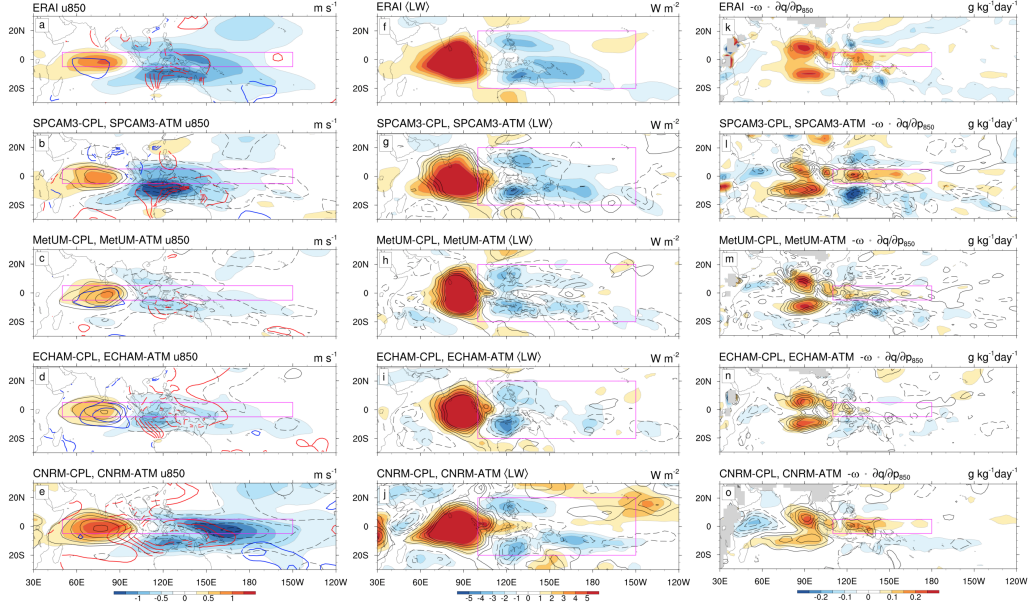


Figure 4. Anomalous 850 hPa zonal wind (a–e), vertically integrated longwave heating (f–j), and 850 hPa vertical moisture advection (k–o) regressed onto 20–100 day filtered rainfall for a 90°E basepoint (i.e., the 80°E–100°E; 15°–15°E area average). Units listed in each panel are per 1 mm day^{−1} of basepoint rainfall. Results for coupled (uncoupled) systems are shaded (contoured; interval as in shaded field). Shaded regions correspond to significance at the 95% confidence interval over most of the domain. Red (blue) contours in a–j are positive (negative) SST contours (units [0.1 K]/[mm day^{−1}]). Magenta boxes denote averaging regions used to compute MJO metrics (see text and Figure 5).

sonal rainfall variability. Similarly, coupling increases MJO period in some CGCMs and reduces it in others. The MJO pattern correlation, east-west power ratio, KW/ER asymmetry, and dry phase intensity metrics all increase with coupling, and are significantly correlated with one another, as shown in Table 2. This suggests that these indices should be thought of as MJO metrics, which characterize MJO fidelity, rather than as process metrics, which measure the magnitude of processes that maintain or propagate MJO convection. For example, consider the case of widespread subsidence east of MJO convection. Chen and Wang (2018) report that the western part of the subsiding region arises from compensating subsidence driven by upper-level divergence associated with Indian Ocean MJO convection, while the eastern part of the subsiding region arises from wake subsidence from the previous MJO event. The dry phase intensity metric, then, is an MJO metric because it combines measures of MJO propagation and upper-level circulation. The low-level poleward flow associated with the dry phase advects mean-state moisture poleward, which is characterized using the meridional advection process metric.

Zonal mean state moisture gradients that promote MJO propagation do not uniformly increase with coupling ($dCWV/dx$ (WP) and $dCWV/dx$ Aus; Fig. 5b). Meridional mean-state moisture gradients, however, uniformly increase with coupling and many of these increases are statistically significant. This unexpected result warrants further consideration. Conventional wisdom holds that constraining CGCM and AGCM simulations of the same model to the same mean-state SST effectively eliminates mean-state CWV differences that affect MJO propagation (e.g., Klingaman & Woolnough, 2014). Instead, our results demonstrate that, despite no change in SST climatology and low-frequency variability, coupled feedbacks consistently yield mean-state CWV patterns that favor MJO propagation (Figure 1i-l). Higher-frequency ocean-atmosphere interactions (i.e., 30-day or shorter timescales) adjust, or rectify onto, the mean-state moisture distribution to favor MJO propagation. This is the result of an asymmetry or non-linearity of moistening processes for positive and negative SST anomalies in coupled models that yield a “rectified” non-zero net moistening. For the atmosphere, the “rectifier effect” can be seen as the net effect of a short or small scale process on a longer or larger scale process (e.g., Denning et al., 1999; Kessler & Kleeman, 2000; Shinoda & Hendon, 2002).

How do coupled feedbacks affect maintenance or propagation of intraseasonal MSE anomalies? Coupled minus uncoupled projections of MSE budget terms (Eq. 1) onto 20–100 day filtered $\langle m \rangle$ and $\frac{\partial \langle m \rangle}{\partial t}$ are shown in Figures 5c and 5d, respectively. Note that,

Table 2. Correlations between MJO skill and descriptor metric across ERAI and the eight simulations. Significance at the 95% (90%) confidence interval is shown in bold (italicized bold) text. Metrics are defined in Sections 3.1 and 3.2.

Metric	Pattern Corr.	EW ratio	Period	Rain Amp.	KW/ER ratio	KW _{max}	ER _{max}	Dry Phase	BL exp.
Pattern Corr.	—	0.66	0.35	-0.30	0.92	0.74	-0.11	0.79	0.25
EW ratio	0.66	—	0.62	0.21	0.75	0.79	0.13	0.33	0.23
Period	0.35	0.62	—	0.07	0.53	0.69	0.57	-0.09	-0.09
Rain Amp.	-0.30	0.21	0.07	—	-0.21	0.28	-0.39	-0.45	-0.37
KW/ER ratio	0.92	0.75	0.53	-0.21	—	0.84	0.02	0.63	0.26
KW _{max}	0.74	0.79	0.69	-0.28	0.84	—	0.49	0.57	0.51
ER _{max}	-0.12	0.13	0.57	-0.39	0.02	-0.49	—	-0.13	0.30
Dry Phase	0.79	0.33	-0.09	-0.45	-0.63	0.57	-0.13	—	0.65
BL exp.	0.25	0.23	-0.09	-0.37	0.26	-0.51	0.30	0.65	—

in contrast to the relative differences plotted in Figure 5a, coupled minus uncoupled MSE projections are plotted as absolute differences. We find that coupling has no consistent effect on $\langle m \rangle$ maintenance, and that the effect of coupling on $\langle m \rangle$ maintenance by vertical MSE advection ($\langle -\omega \frac{\partial m}{\partial p} \rangle$; VADV) and surface fluxes may be sensitive to whether the AGCM is coupled to a 3D or 1D ocean (i.e., yellow bars in Figure 5c). We elaborate on these differences in Section 6. Changes in processes that support $\frac{\partial \langle m \rangle}{\partial t}$ lend further weight to the argument that mean-state moisture gradient changes improve MJO propagation in the CGCMs. Horizontal moisture advection ($\langle -V \cdot \nabla m \rangle$; HADV) significantly enhances $\frac{\partial \langle m \rangle}{\partial t}$ and MJO propagation in all coupled simulations. By decomposing the advection term into its zonal ($\langle -u \frac{\partial m}{\partial x} \rangle$; u-HADV) and meridional ($\langle -v \frac{\partial m}{\partial y} \rangle$; v-HADV) components, it is clear that enhanced meridional MSE advection is the common process responsible for enhanced MJO propagation in the CGCMs. Furthermore, close inspection of Figure 5d reveals that meridional MSE advection increases are larger than increases in nearly all other terms. The sole exception is vertical MSE advection in SPCAM3-CPL. We consider this difference further in Section 6. Coupling uniformly reduces surface flux contributions to MSE tendency, thereby inhibiting, rather than encouraging, MJO eastward propagation. The combination of mean-state low-level westerlies and stronger MJO-associated low-level easterlies in CGCMs reduces the total wind speed and surface fluxes east of MJO convection in CGCMs.

4 Cause or effect: MJO and mean-state moisture

The above analysis demonstrates the connection between improved MJO propagation and sharpened meridional moisture gradients in CGCMs, but does not provide any insight into causality. It is possible that coupled feedbacks alter MJO convection and circulations to enhance the equatorward CWV gradients, so that sharpened meridional moisture gradients are a consequence, rather than a cause, of improved MJO propagation.

To test this hypothesis, we used a version of the Real-time Multivariate MJO indices (RMM; Wheeler & Hendon, 2004) adapted for climate-length simulations (Madden-Julian Oscillation Working Group, 2009) to identify MJO and non-MJO periods. The RMM indices are obtained through the multivariate empirical orthogonal function (EOF) decomposition of 20–100 day filtered outgoing longwave radiation (OLR) and zonal wind at 200 and 850 hPa. The two leading EOFs capture the eastward propagating MJO; their

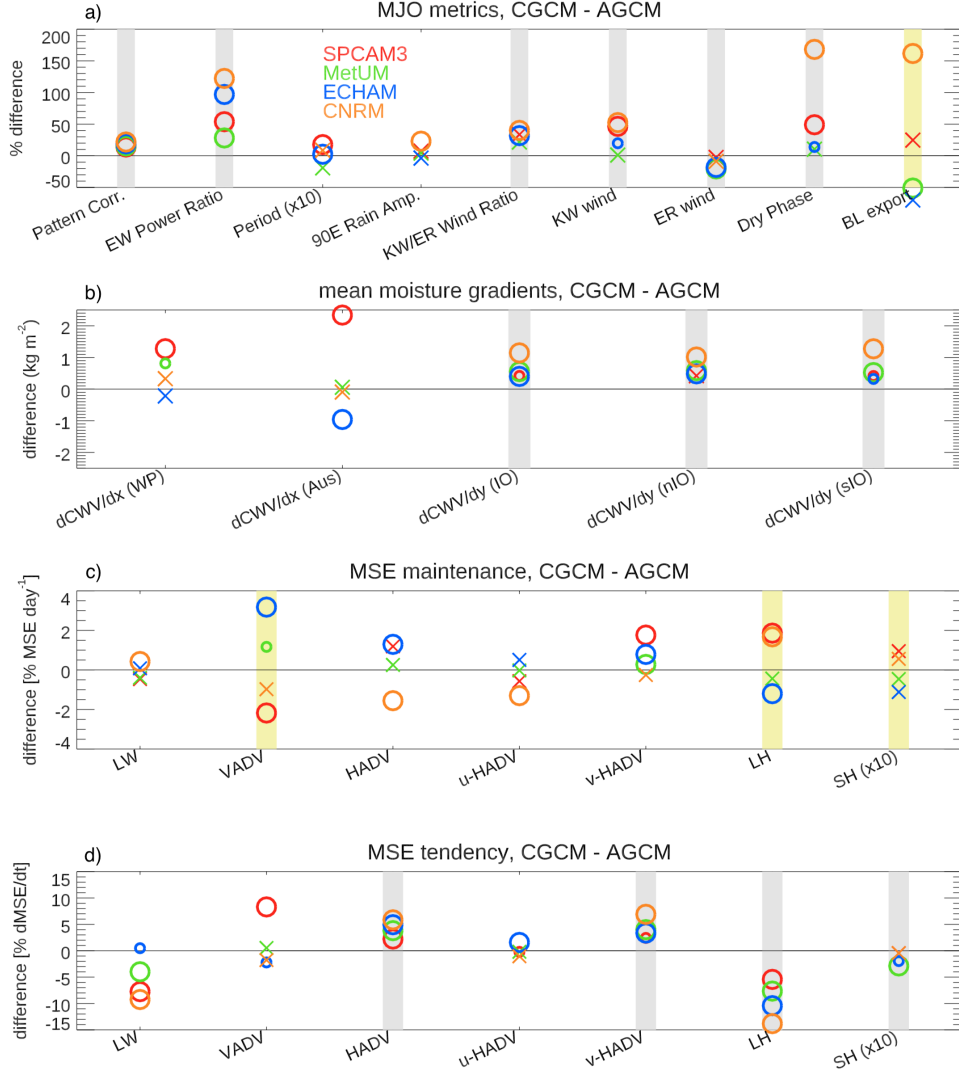


Figure 5. CGCM minus AGCM differences for a) MJO descriptive metrics, b) mean state CWV gradients, c) MSE maintenance and d) MSE tendency by MSE budget terms (Eq. 1). Same-signed changes across all four models are denoted with gray background stripes. Changes that differ according to ocean model (i.e., 3D or 1D) are denoted with yellow background stripes. Significance at the 90% and 95% confidence levels are denoted with small and large open circles, respectively, while \times indicates differences that are not significant. For a) and b), significance was assessed with a student's t-test based on multiple three- and one-year data subsets, respectively. In c) and d), significance was tested with a student's t-test based on the area-averaged regression coefficients for the domain plotted in Figure 4.

principal component (PC) time series can quantify MJO phase and amplitude. We computed the RMM EOFs from NOAA daily mean OLR (Liebmann, 1996) and ERAI winds and projected these onto model output, to obtain RMM indices for each CGCM. The PC timeseries are normalized, and MJO and non-MJO periods are identified as periods when the RMM amplitude ($A = \sqrt{PC_1^2 + PC_2^2}$) is greater than or less than one, respectively.

To determine if the improved MJO in the CGCM is responsible for the sharpened meridional moisture gradient, we computed the average CWV difference for MJO and non-MJO periods in the CGCM and compared it to the average CWV difference between the CGCM and AGCM. MJO and non-MJO CWV differences were computed for each month (November–April) and then averaged across the entire season to account for seasonal shifts in MJO amplitude that arose in some CGCMs. The results are shown in Figure 6a–e. Shading (CGCM MJO minus non-MJO) and contours (CGCM minus AGCM) are plotted using the same contour interval to emphasise the relative magnitudes of the two differences. Except for CNRM, MJO minus non-MJO CWV differences are much smaller than coupled minus uncoupled CWV differences. Pattern correlations between the two fields for Indian Ocean and western Pacific regions are listed in each panel. Negative or small positive correlations for the Indian Ocean suggest that the MJO either weakly disperses moisture away from the Equator, or has little net effect on the CWV distribution.

In the western Pacific, MJO minus non-MJO differences (shading) for ERAI and CNRM-CPL bear a strong resemblance to El Niño conditions, which are known to influence MJO propagation (Pohl & Matthews, 2007; DeMott et al., 2018). To remove ENSO influences, we repeated the analysis with 100 day high-pass filtered data (Figure 6f–j), which reduces MJO minus non-MJO differences. Although the western Pacific and Indian Ocean correlations increase for SPCAM3-CPL and CNRM-CPL, respectively, the small magnitude of MJO minus non-MJO changes in these regions ($<1 \text{ kg m}^{-2}$) is likely insufficient to explain the CGCM minus AGCM CWV differences. We therefore reject the hypothesis that the improved MJO in the CGCMs causes enhanced equatorward moisture gradients.

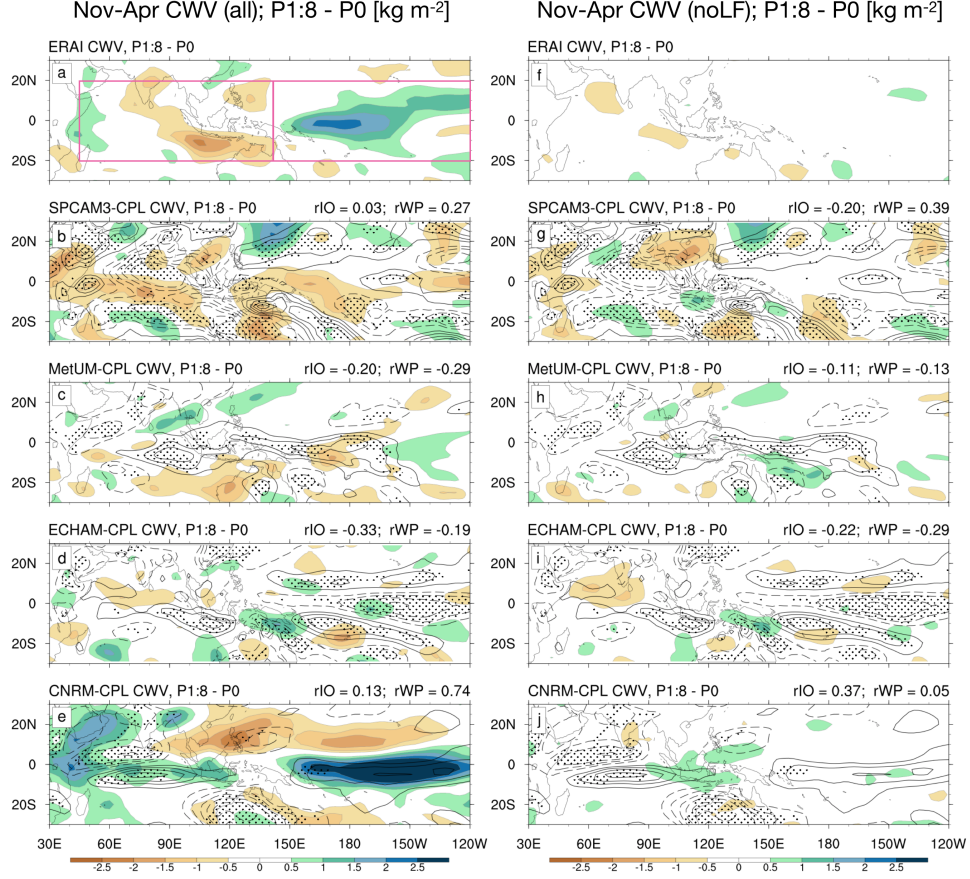


Figure 6. November–April CWV differences for CGCM MJO periods ($RMM > 1$) and non-MJO periods ($RMM < 1$) (shading; shaded values correspond to 95% or greater significance over most of domain) and CGCM minus AGCM CWV differences (contours; negative values dashed and zero contour omitted; 95% significance stippled). Shading and contours are plotted with the same contour interval. CGCM MJO minus non-MJO CWV differences for unfiltered (100 day high-pass filtered) input are plotted on the left (right). Pattern correlations for Indian Ocean and western Pacific Ocean regions (magenta boxes in panel a; rIO and rWP, respectively) are listed on each panel.

5 How do ocean feedbacks rectify onto mean state CWV?

5.1 Evaluation of processes that could affect CWV differences

Understanding how coupling leads to mean-state moisture changes in the four models is key to understanding how coupling improves MJO propagation. While the models differ in physical parameterizations and ocean models (Table 1), they uniformly exhibit sharpened meridional moisture gradients and improved MJO propagation with coupling. This raises the question of whether the models arrive at their coupled mean states through a common process or a unique process in each model.

We examined several processes that might be linked to the mean-state moisture differences. The processes, and the models whose process change is correlated with the CWV change (shown in parentheses, plus any relevant references) are: enhanced Hadley circulation over the Warm Pool (SPCAM3-CPL, MetUM-CPL); reduced vertical component of gross moist stability (ECHAM-CPL; Neelin, Held, and Cook (1987); Benedict, Maloney, Sobel, Frierson, and Donner (2013)); enhanced support of convection by surface latent heat fluxes (SPCAM3-CPL, CNRM-CPL; Riley Dellaripa and Maloney (2015); DeMott et al. (2016)); and enhanced longwave radiative feedbacks (none; Del Genio and Chen (2015)). These findings would support the “model-dependent pathway” paradigm for mean state CWV changes with coupling, but remain unsatisfying since they generally offer few insights into how ocean feedbacks affect a given process.

5.2 Insights from Q_2 profiles for understanding CWV differences

A new method for analyzing the response of convection to coupling reveals a common process that may explain the CGCM-minus-AGCM CWV differences. First, we constructed CGCM rainfall rate probability distribution functions (PDFs) for warm and cold daily mean SSTA periods for the domain 15°S–15°N and 50°E–180°E (Figure 7a; results for 20°S–20°N and 30°E–240°E are virtually identical). Non-rainy days are excluded by estimating the minimum allowable rainfall rate (≈ 0.05 mm day⁻¹) that yields a first-bin frequency that matches an estimated first-bin frequency obtained by extrapolating the PDF curve from the second-through-fourth bins. The warm-minus-cold PDF differences (Figure 7c) reveal model-dependent changes to the PDFs: ERAI, SPCAM3-CPL, and CNRM-CPL shift toward heavier rainfall rates during warm SSTA periods, while MetUM-CPL and ECHAM-CPL contract toward moderate rainfall rates. Rain-

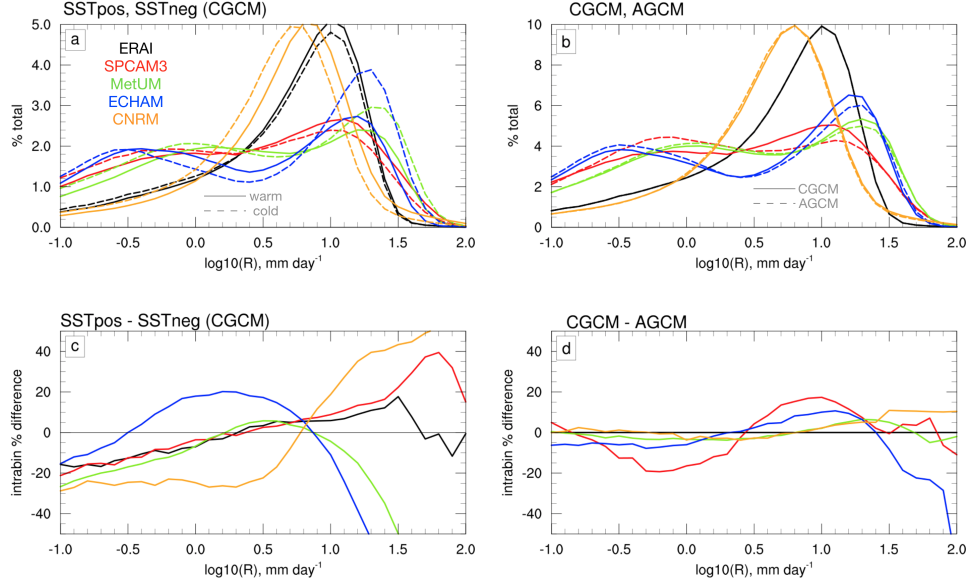


Figure 7. Probability distribution functions (PDFs) of a) $\log_{10}R$ for ERAI and CGCM warm (solid) and cold (dashed) SST anomalies (SSTA) and b) CGCM (solid) and AGCM (dashed) simulations. PDF differences for c) ERAI and CGCM warm - cold SSTA ($\Delta f = 100 \cdot (f_+ - f_-)/f_-$ where f is the fraction of observations per rainfall rate bin and $+$ and $-$ subscripts refer to warm and cold SSTA, respectively) and d) CGCM - AGCM simulations ($\Delta f_{CPL-ATM} = 100 \cdot (f_{CPL} - f_{ATM})/f_{ATM}$ where CPL and ATM subscripts refer to CGCM and AGCM simulations, respectively). Data are drawn from ocean-only points from 15°S – 15°N and 50°E – 180°E . All distribution differences in c) and d) were tested with a Kolmogorov-Smirnov test and are significant at the 95% confidence level.

fall rate PDFs for CGCMs and AGCMs, and their intra-bin differences, are shown for comparison in Figures 7b and 7d, respectively. In general, CGCM-minus-AGCM PDF differences (Figure 7d) are smaller than the warm-minus-cold SSTA differences (Figure 7c).

We next analyzed Yanai’s “apparent moisture sink,” Q_2 (e.g., subgrid-scale or unresolved moistening by convection; Yanai et al., 1973) conditioned by rainfall rate and SSTA for ERAI and the models. The results, plotted as $-Q_2/L_v$ with units of $\text{g kg}^{-1} \text{ day}^{-1}$ so that positive values represent moistening, are shown in Figure 8. November–April mean $-Q_2/L_v$ profiles from the CGCMs (gray contours) demonstrate the broad similarity of convective moistening characteristics for ERAI and all models: convection (via parameterized physics) moistens low levels and dries upper levels at low rainfall rates, while the opposite is observed at high rainfall rates. The warm-minus-cold $-Q_2/L_v$ difference

profiles (shading in Figure 8; left column), however, are not consistent across all models. We are especially interested in low-level convective moistening (i.e., below about 700 hPa) since MJO propagation via horizontal moisture advection is most sensitive to lower-tropospheric moisture patterns (e.g., Gonzalez & Jiang, 2017). For ERAI, SPCAM3-CPL, and CNRM-CPL, low-level convective moistening above the atmospheric mixed layer (above 925 hPa) is enhanced for nearly all rainfall rates during warm SSTA periods, but is reduced for MetUM-CPL and ECHAM-CPL. This would appear to reinforce the model-dependent pathway for CWV changes with coupling, but as we demonstrate next, it is the combination of warm-minus-cold rainrate PDFs and warm-minus-cold $-Q_2/L_v$ profiles that explains the uniform increase in equatorial CWV in all four models.

The warm-minus-cold $-Q_2/L_v$ differences (Figure 8; left column) weight equally the warm and cold SSTA $-Q_2/L_v$ averages at each rainfall rate bin. However the distribution of rainfall rates for warm and cold SSTA periods is unequal (Figure 7b). To understand how coupling affects convective moistening, we must account for both differences, by multiplying the warm-minus-cold $-Q_2/L_v$ difference profiles (Figure 8; left column) by their respective intra-bin rainfall rate PDF differences (Figure 7b); Figure 8 (center column) shows the product. For ERAI, SPCAM3-CPL, and CNRM-CPL, more frequent heavy rainfall and less frequent light rainfall during warm SSTA periods yields less low-level moistening at low rainfall rates, and more low-level moistening at high rainfall rates. In contrast, for MetUM-CPL and ECHAM-CPL, the reduced frequency of heavy rainfall rates for warm SSTA reduces low-level drying during warm SSTA periods and increases low-level moistening during cold SSTA periods. The net effect for all four models is an *increase* in low-level convective moistening at high rainfall rates (i.e., $R \geq 5$ mm day⁻¹). Note that we would get the same result had we instead analyzed cold-minus-warm SSTA differences. These results, therefore, summarize the net effect of coupling, not simply the effect of warm SSTAs.

While the warm-minus-cold SSTA-weighted $-Q_2/L_v$ differences (Figure 8; center column) illustrate the essential effects of ocean coupled feedbacks on convective moistening, the results do not account for the overall distribution of rainfall rates. The final step in the analysis is to multiply the warm-minus-cold SSTA-weighted $-Q_2/L_v$ differences (Figure 8; center column) by the normalized ERAI or CGCM rainfall rate PDF (Figure 7c), where the PDF is normalized by its maximum value. This step reduces the magnitude of $-Q_2/L_v$ differences at very low and very high rainfall rates (Figure 8; right

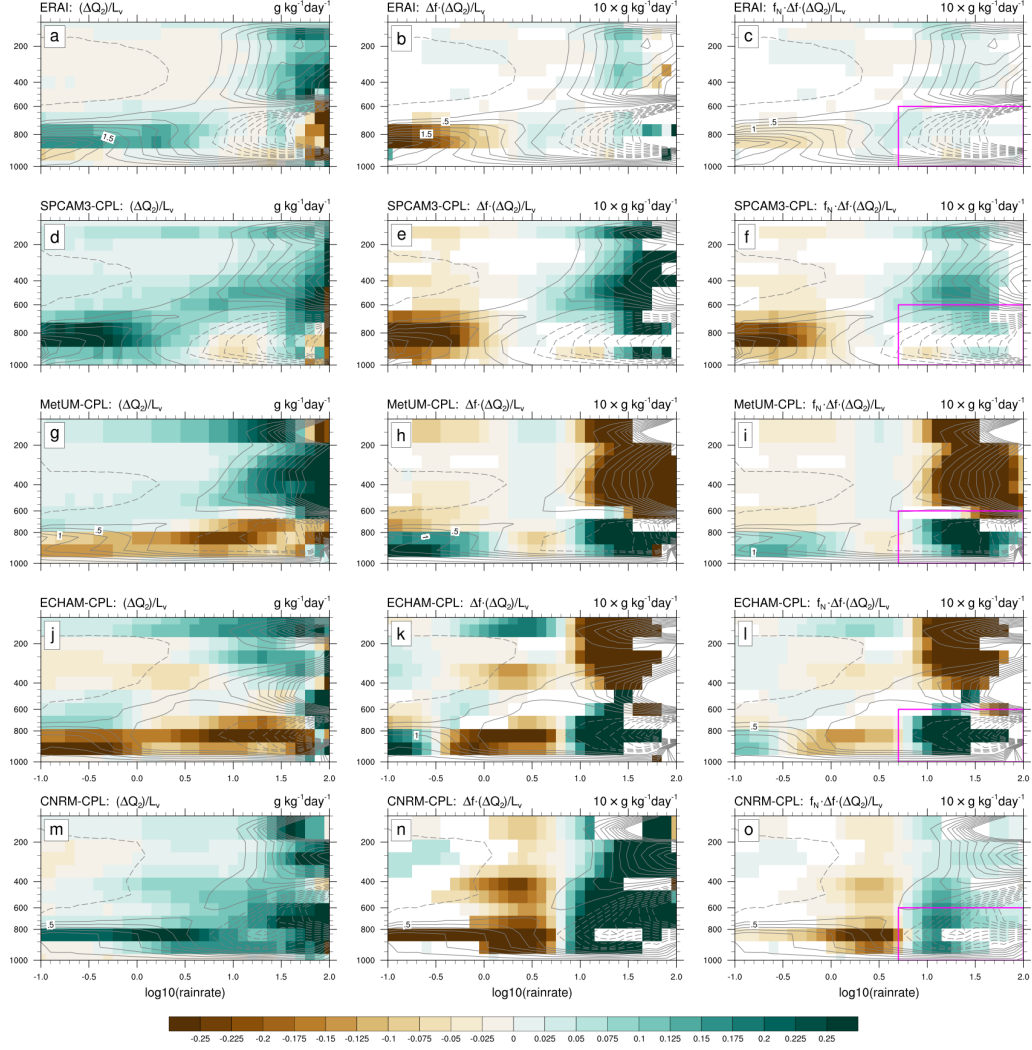


Figure 8. Average $-Q_2/L_v$ vertical profiles binned by rainfall rate (solid) and left the $-Q_2/L_v$ difference for warm-minus-cold SSTA (shading; $-\Delta Q_2/L_v$); center) $-\Delta Q_2/L_v$ (left column) multiplied by Δf (Figure 7c); and right) $\Delta f \cdot (-\Delta Q_2/L_v)$ (center column) multiplied by the normalized f_{CPL} (Figure 7b), f_N . Warm-minus-cold $-\Delta Q_2/L_v$ differences in center and right columns are plotted only where statistically significant at the 95% confidence interval. Magenta boxes in right column highlight moistening at $R > 5 \text{ mm day}^{-1}$ and below 600 hPa. Data are drawn from same domain as in Figure 7.

column), but otherwise does not change the rainfall rates associated with the largest moistening differences. Figure 8 (center and right columns) illustrates the rectification of ocean feedbacks onto moistening by parameterized physics.

5.3 The relationship between SST- and rainfall rate-conditioned $-Q_2/L_v$ and mean state CWV differences

The above suggests two criteria for coupled feedbacks to enhance local low-level convective moistening: (a) the region should be dominated by rainfall rates greater than about 5 mm day^{-1} ; (b) these heavy rainfall rate regions should exhibit more frequent SSTAs whose sign (positive or negative) is consistent with enhanced low-level moistening for that model.

To assess whether the above criteria apply to these models, we plot maps of the frequency of $R > 5 \text{ mm day}^{-1}$ for each CGCM (left column of Figure 9). The frequency of $R > 5 \text{ mm day}^{-1}$ maximizes near the Equator, satisfying the first criterion for enhanced low-level moistening by unresolved convective processes. Whether these regions experience enhanced or reduced moistening, however, depends on whether they are dominated by warm SSTAs (SPCAM3-CPL and CNRM-CPL), or cold SSTAs (MetUM-CPL and ECHAM-CPL). Maps of the frequency difference for warm and cold SSTAs during heavy rain condition (center column of Figure 9) show that for SPCAM3-CPL and CNRM-CPL, the heavy rain-dominated regions are dominated by warm SSTAs, consistent with enhanced low-level moistening by convection. Although the regions of frequent heavy rainfall and frequent warm SSTA do not everywhere agree with CWV differences, this analysis does not consider circulation effects on CWV that may modulate the overall CWV distribution. Nevertheless, the spatial distribution of the frequency of heavy rainfall and warm SSTAs suggest that changes in low-level convective moistening are responsible for the changes in CWV between CGCM and AGCM simulations for these two models. For MetUM-CPL and ECHAM-CPL, the frequent heavy-rain regions are dominated by *cold* SSTAs, which is consistent with the enhanced equatorial low-level moistening and CWV changes for these two models. Daily SST variability is generally large in the regions of frequent heavy rainfall (e.g., DeMott et al., 2016), which may also help localize the ocean-to-convective moistening feedback.

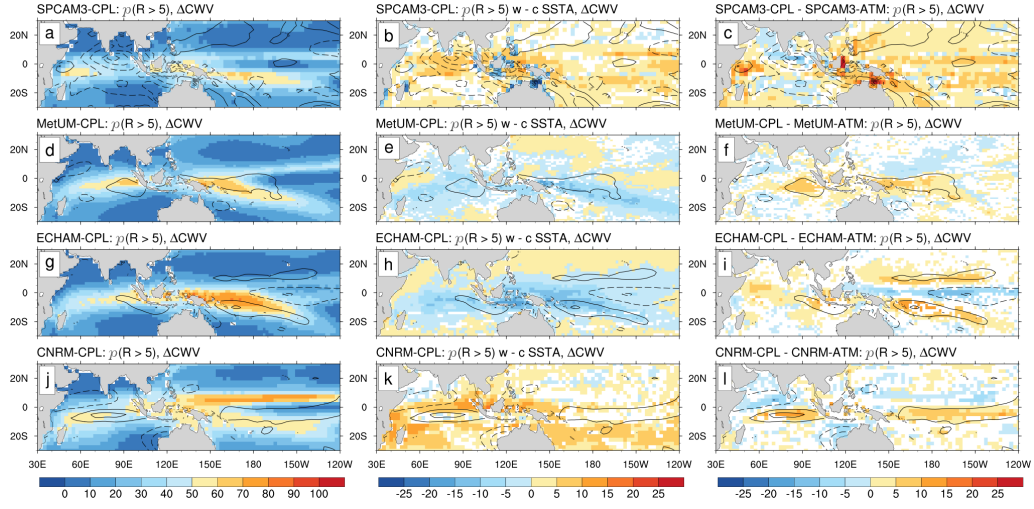


Figure 9. November–April frequency of left) $R \geq 5 \text{ mm day}^{-1}$; center) warm-minus-cold SSTA frequencies of $R \geq 5 \text{ mm day}^{-1}$; and right) CGCM-minus-AGCM frequencies of $R \geq 5 \text{ mm day}^{-1}$. The coupled minus uncoupled CWV difference (spatially smoothed) is contoured (interval is 1 kg m^{-2} ; negative values are dashed and zero contour is omitted). In center and right columns, frequency differences are plotted only where rainfall distributions are statistically significant at the 95% confidence interval, as determined by a Kolmogorov-Smirnov test.

The imprint of coupled feedbacks on convective moistening is considered for CGCM-minus-AGCM CWV differences. The difference in heavy rain frequency between CGCMs and AGCMs (right column of Figure 9) and CWV differences are well-correlated ($r \geq 0.7$ for the plotted domain). The close relationship between tropical rainfall and CWV is well known (e.g., Bretherton et al., 2005; Thayer-Calder & Randall, 2009; Neena et al., 2014), but it can be difficult to infer if convection is responsible for CWV patterns or vice versa: convection that results in moderate-to-high rainfall rates moistens the atmosphere, but a moist atmosphere favors development of more intense convection. Our analysis, however, suggests that the response of convection to ocean feedbacks plays a role in shaping the coupled minus uncoupled CWV differences.

6 Synthesis and Discussion

We have demonstrated that the common factor for improved MJO simulation skill with coupling is the sharper equatorward moisture gradients across the Warm Pool, which enhances tropospheric moistening by meridional moisture advection east of MJO convection. The sharper moisture gradients in CGCMs arise from coupled feedbacks that enhance low-level convective moistening for rainfall rates greater than about 5 mm day^{-1} ; this enhancement is most frequently observed near the Equator. Next, we consider how atmospheric and oceanic model physics jointly regulate tropospheric moistening, and whether these interactions are consistent with those inferred from observation-based estimates.

6.1 Ocean feedbacks and convective activity

We first consider interactions among the ocean, convection, and free-tropospheric moisture in MetUM-CPL and ECHAM-CPL. The cumulus parameterization in each model employs a CAPE-based closure assumption: when temperature and moisture perturbations near the surface and aloft generate positive CAPE, convection is initiated to consume CAPE and maintain a neutrally stable environment. Because of weak tropical temperature gradients, CAPE in the tropics is highly sensitive to surface temperature perturbations (Williams, 1994). Rules for convective initiation may also play a role. For example, in MetUM, convection is initiated when the temperature profile at the lifted condensation level becomes unstable, regardless of conditions aloft. In MetUM-CPL and ECHAM-CPL, compared to cold SSTAs, warm SSTAs generate larger CAPE, requiring more or stronger convection to neutralize the instability. We hypothesize that this increased “de-

mand” for deep convection above warm SSTAs is the cause for relatively stronger upper-level moistening and weaker low-level moistening for warm SSTAs at all rainfall rates.

MetUM-CPL and ECHAM-CPL are both coupled to 1D ocean mixed layer models with fine vertical resolution (≈ 1 m in the upper 10 m) and sub-daily coupling designed to represent the large SST diurnal cycle during suppressed conditions (e.g., Kawai & Wada, 2007). The SST diurnal cycle rectifies onto subseasonal scales (Bernie et al., 2005; Shinoda, 2005), so that the Warm Pool daily SSTA distributions in MetUM-CPL and ECHAM-CPL are positively skewed (Figure 10). The transition from convectively suppressed to disturbed conditions in MetUM-CPL and ECHAM-CPL would coincide with rapid SST warming in response to strong surface heating, reduced evaporative cooling (from reduced wind speed), and ocean mixed layer shoaling (Figure 11). The rapid SST warming would quickly generate CAPE and initiate convection, even though the mid-troposphere is typically too dry to support deep convective moistening at these rainfall rates (Thayer-Calder & Randall, 2009; Kim et al., 2009). As large-scale circulations moisten mid-levels via moisture advection, increasing MJO-associated surface wind anomalies and, potentially, convectively driven wind gusts will cool the upper ocean, so that by the time convection has organized into a large-scale system with heavy rainfall, SSTs will have cooled. In these cold SSTA conditions, plumes originating from the boundary layer will be less buoyant and detrain moisture at lower levels than their warm SSTA counterparts, thereby enhancing low-level moisture.

SPCAM3-CPL and CNRM-CPL differ from MetUM-CPL and ECHAM-CPL in that neither employ CAPE-based closure assumptions in their cumulus parameterizations, and both are coupled to 3D ocean models with coarse (≈ 10 m) upper-ocean vertical resolution. Convection in SPCAM3-CPL is explicitly simulated with a continuously running two-dimensional cloud-permitting model embedded in each GCM grid column. The convection scheme in CNRM-CPL employs a moisture convergence closure assumption. These treatments may reduce the sensitivity of convective initiation to SST perturbations, allowing CAPE to build up before convection is initiated, thus favoring the shift toward higher rainfall rates during warm SSTA periods (Figure 7c). It is also possible that the coarse upper-ocean vertical resolution in these models yields a smaller SST tendency than that in MetUM-CPL or ECHAM-CPL. This reduced warming rate could subtly shift the phasing of maximum SST with respect to convection so that it more closely aligns with heavier rainfall rates.

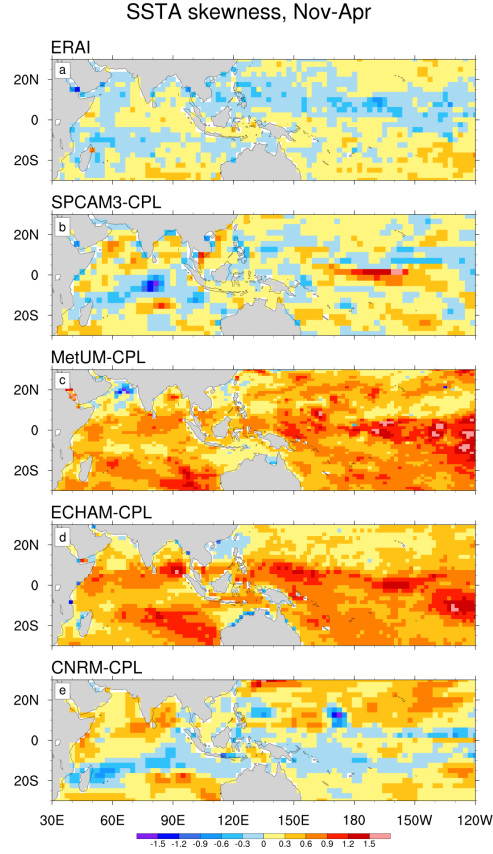


Figure 10. SSTA skewness, defined as the third moment of the SSTA distribution, for CGCMs.

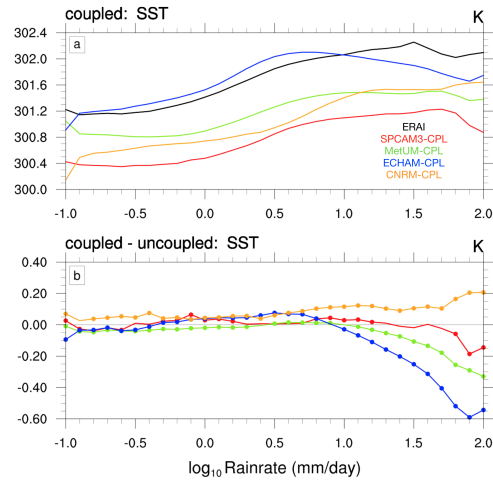


Figure 11. a) Mean SST as a function of rainfall rate for CGCMs and b) mean SST differences for CGCMs minus AGCMs (dots indicate differences are significant at the 95% confidence interval).

6.2 Coupled feedbacks to the convection–column humidity relationship

The above discussion implicitly invokes our understanding that rainfall intensity is regulated by the mixing of cloud and environmental properties through detrainment and entrainment (e.g., de Rooy et al., 2012). Because bulk mixing rates for these processes are difficult to measure, in GCMs they are often tuned to achieve realistic cloud-top height distributions, temperature and humidity profiles, or rainfall climatology. While knowledge of entrainment processes in a GCM can help diagnose the spectrum of convective variability (DeMott et al., 2007; Thayer-Calder & Randall, 2009; Klingaman & Woolnough, 2014), other factors, such as stability, moisture advection, and the interactions of cloud microphysical properties with convective heating also regulate the sensitivity of rainfall intensity to column humidity ([e.g., Klingaman et al., 2015]).

To better understand the net effect of these interactions, we examined how rainfall rate depends on the CWV saturation fraction (Bretherton et al., 2004; Neelin et al., 2009) in each GCM. In the tropics, the frequency of heavy rainfall increases non-linearly with the column saturation fraction, defined as the ratio of column water vapor to saturation column water vapor. CGCM joint PDFs of CWV fraction and rainfall rate are plotted with contours in Figure 12. The “precipitation uptick” (i.e., where rainfall rate increases rapidly as a function of CWV fraction) in SPCAM3-CPL, MetUM-CPL, and ECHAM-CPL occurs near the 0.8 CWV fraction, consistent with analysis of observations (Bretherton et al., 2004; Neelin et al., 2009). For CNRM-CPL, the uptick is delayed until 0.95 CWV fraction, suggesting that deep convection in that model is overly sensitive to column moisture.

The effect of coupling on the convection–column humidity relationship is shown by plotting the joint PDF difference for warm and cold SSTA periods (shading in the left column of Figure 12). Compared to cold SSTA PDFs, warm SSTA PDFs in SPCAM3-CPL and CNRM-CPL are shifted toward lower saturation fractions, suggesting a reduced critical saturation fraction for heavy rainfall for warm SSTA periods. In MetUM-CPL and ECHAM-CPL, the warm SSTA PDFs shift toward lower saturation fractions at light rainfall rates, but also shift away from heavy rainfall rates for most saturation fraction bins (consistent with the rainfall rate PDF difference shown in Figure 7c). This suggests that convection initiation in MetUM-CPL and ECHAM-CPL may be overly sensitive to SSTAs, while rainfall intensity remains sensitive to saturation fraction as seen in the re-

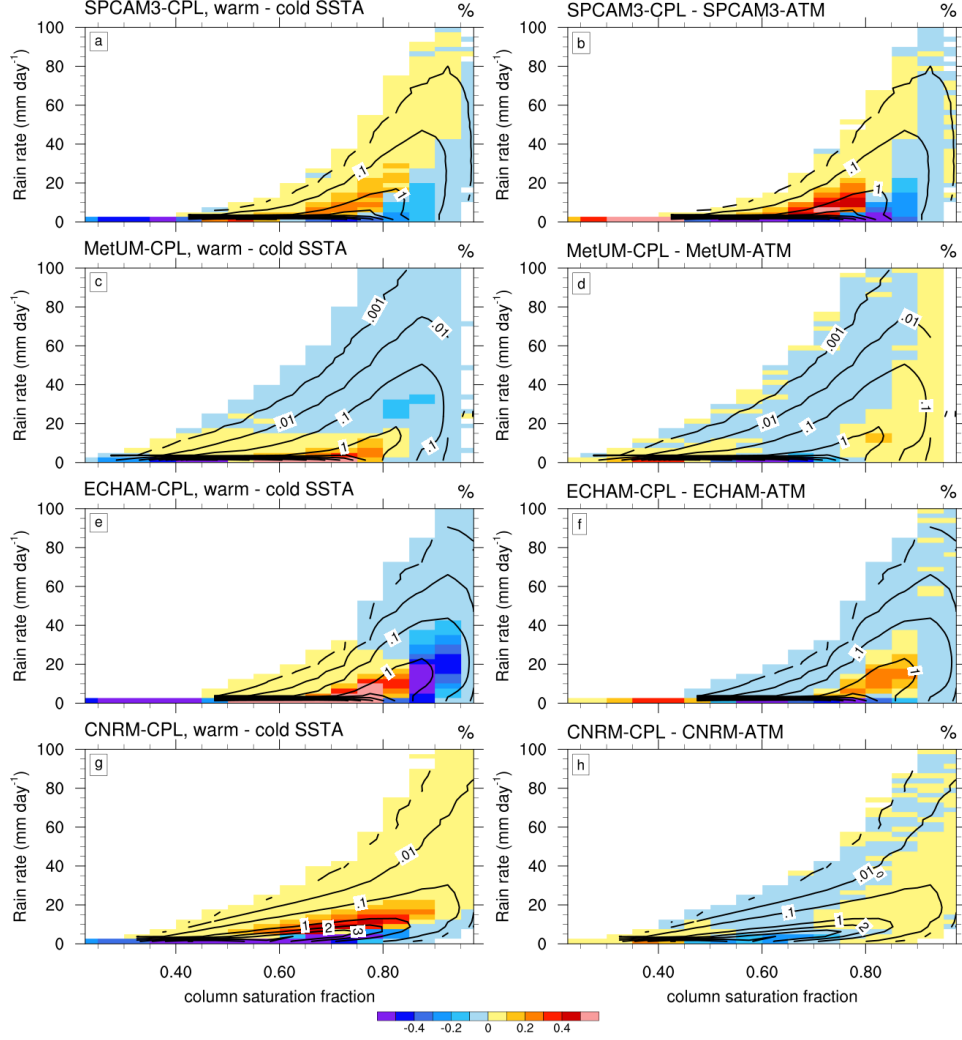


Figure 12. November–April joint PDFs of daily column saturation fraction and daily mean rainfall rate for CGCMs (contours; see text for definition) and left) the joint PDF difference for warm-minus-cold SSTA periods (shading) and right) the joint PDF difference for CGCM minus AGCM simulations (shading). Ocean-only data are compiled over the Warm Pool (20°S–20°N; 30°E–240°E).

duced occurrence of high rainfall rates for warm SSTA periods. This is consistent with our argument that convection initiates too readily (i.e., in a too-dry environment) with warm SSTAs in these models, and the convective plumes quickly lose buoyancy as they entrain dry environmental air.

The PDF differences for coupled minus uncoupled simulations (Figure 12; right column) are difficult to interpret. At a minimum, they illustrate that the net effects of coupled feedbacks on the convection–column humidity relationship are highly model dependent. This sensitivity is likely rooted in large-scale circulation changes or other feedbacks beyond those directly related to coupling.

6.3 The role of surface fluxes

The atmosphere senses SST perturbations through their effects on surface fluxes. These fluxes are sources of atmospheric boundary-layer buoyancy, which regulates the depth of convective plumes originating from the boundary layer. Although the latent heat flux is an order of magnitude larger than the sensible heat flux, its contribution to boundary-layer buoyancy (via the effect on water vapor density) is roughly comparable to that of the sensible heat flux. For a given wind speed, the latent heat flux is primarily governed by the specific humidity of near-surface air, while the sensible heat flux is more sensitive to the SST (DeMott et al., 2014; Yokoi et al., 2014). From the perspective of boundary-layer buoyancy budgets, SST perturbations are more directly communicated to the atmosphere through the sensible heat flux (e.g., Yang, 2018). Both fluxes contribute to the vertical ascent of convective plumes through converting boundary-layer available potential energy to kinetic energy. Once the plumes reach their lifted condensation level, the release of energy by condensation of oceanic water vapor increases plume buoyancy. Both the boundary-layer buoyancy and the latent heat release from the condensation of previously evaporated surface water will be greater for plumes originating over warm SSTAs than over cold SSTAs. Warm SSTA plumes will rise farther, and detrain their moisture higher, than cold SSTA plumes.

DeMott et al. (2016) and Gao, Klingaman, DeMott, and Hsu (2018) found that observed tropical intraseasonal SST perturbations to surface fluxes directly contribute up to 1–2% of $\langle m \rangle$ and 10–20% of $\frac{\partial \langle m \rangle}{\partial t}$ across the Warm Pool. Our findings herein that coupled surface fluxes increase the efficiency of convective moistening at high rainfall rates,

and that this more efficient moistening occurs near the Equator, offer a process-level perspective of the SST *direct* effects reported in DeMott et al. (2016) and Gao et al. (2018). The more important feedback for MJO propagation, however, is the *indirect* effect of SST perturbations on MJO propagation through its regulation of the mean-state moisture distribution.

Another point worth discussing is the role of low-level moistening from vertical moisture advection driven by boundary-layer convergence. Our results clearly demonstrate that equatorial boundary-layer moisture export does not uniformly increase with coupling. The decrease in boundary-layer moisture pumping with coupling seen in MetUM-CPL and ECHAM-CPL may be linked to the rapid decline in SSTA with heavy rainfall in those models (Figure 11b), which could limit warm SST contributions to boundary layer convergence during convective build-up periods. For ECHAM-CPL, the “flattening” (vs sharpening) of the meridional moisture gradient in the western Pacific (Figure 1k), and subsequent reduction of meridional moisture advection, may compound the issue. SPCAM3-CPL and CNRM-CPL exhibit coupled moistening characteristics more similar to those observed in ERAI, and they each exhibit increases in boundary layer moisture export with coupling. This provides a modicum of support for the idea that increased boundary-layer moisture export is one reason why MJO propagation improves with coupling, but this topic requires further investigation using observations and coupled reanalyses. Applying the methods developed herein to a larger collection of models with various ocean model configurations could help clarify this issue.

6.4 Ocean coupling–mean state feedbacks in models and ERAI

The final point to consider is whether the ocean feedbacks to convective moistening and mean-state moisture patterns in models are consistent with those in observations. We address this point by revisiting Figure 8. Warm-minus-cold SSTA $-Q_2/L_v$ profiles for SPCAM3-CPL and CNRM-CPL are most similar to those for ERAI (left column), but also exhibit larger SSTA-weighted low-level moistening and drying differences (center and right columns). Low-level moistening differences in MetUM-CPL and ECHAM-CPL are even larger. Are the larger coupled feedbacks in models an indication that ocean coupling acts a crutch for MJO simulation? The muted coupled feedback signature in ERAI in the right column of Figure 8 is largely a consequence of the rarity of high rainfall rates diagnosed by ERAI which, as previously discussed, may be underestimated. Another con-

sideration is that ERAI is an uncoupled data assimilation product, and not an observational product. While $-Q_2/L_v$ can be estimated from oceanic in situ observations collected with triangular or rectangular sounding arrays, these arrays are usually only available during relatively short field campaigns and do not collect enough samples to allow subsetting of $-Q_2/L_v$ by rainfall rate and SSTA. Repeating this analysis with other reanalysis products would help characterize the sensitivity of SSTA-conditioned $-Q_2/L_v$ to the assimilating model.

7 Summary and Conclusions

The role of intraseasonal SST perturbations for MJO eastward propagation was studied with 20–25 year coupled and uncoupled simulations of four different GCMs. Monthly mean SST from each coupled model was prescribed to its respective uncoupled simulation to ensure identical SST mean state and low-frequency variability for each coupled-uncoupled simulation pair. As expected, coupling improved MJO eastward propagation beyond the Maritime Continent in all four models, demonstrating the non-negligible role of sub-monthly SST perturbations for MJO simulation fidelity. The challenge for understanding this result requires reconciling the following: SST perturbations are communicated to the atmosphere through their effects on surface fluxes, yet surface fluxes play only a minor role in the maintenance and propagation of MJO convection. As in observations, MSE budget analyses of the simulated MJO reveal that, to a first order, MJO maintenance and propagation in all eight simulations are maintained by longwave radiative heating and horizontal moisture advection, respectively.

Further analysis revealed that, despite the identical SST climatology in each coupled and uncoupled simulation pair, coupling improves MJO simulation by uniformly sharpening mean state zonal and meridional moisture gradients to enhance advection of the mean-state moisture by the anomalous wind. Improved MJO fidelity in the coupled simulations is uniformly the result of sharper meridional moisture gradients driven by enhanced equatorial CWV (or relatively smaller CWV reduction on the Equator, as in SPCAM3-CPL). The sharper CWV equatorward gradient yields enhanced moistening by poleward flow east of MJO convection and extended eastward propagation of MJO convection compared to uncoupled simulations.

Daily mean CWV averaged over all eight phases of the Wheeler-Hendon MJO RMM index (Wheeler & Hendon, 2004) during MJO active periods (i.e., RMM amplitude > 1) confirms that the MJO does not sharpen meridional CWV gradients. Mechanisms that might explain the sharper meridional gradients in the CGCMs, such as enhanced Warm Pool Hadley circulation or surface flux feedbacks to equatorial convection, are not uniformly observed across models. Instead, SST perturbations in coupled simulations yield different rainfall rate PDFs during warm and cold SSTA periods whose net effect is enhanced low-level convective moistening at high rainfall rates. The intersection of regions dominated by moderately high rainfall rates ($R > 5 \text{ mm day}^{-1}$) and SST anomaly patterns that favor enhanced low-level moistening in each model is found near the Equator. Hence, the sharper moisture gradients that facilitate MJO propagation in coupled simulations are a consequence of oceanic regulation of low-level moistening by unresolved convective processes.

The changes in low-level moistening with ocean feedbacks are sensitive to parameterized processes that regulate convective initiation and entrainment of environmental air. In our study, the CAPE-based closure schemes in MetUM-CPL and ECHAM-CPL yield *reduced* low-level moistening (i.e., relative drying) during warm SSTA periods at all rainfall rates. In contrast, super-parameterized convection in SPCAM3-CPL and the moisture-convergence closure assumption in the CRNM-CPL convective parameterization yield *enhanced* low-level moistening for all rainfall rates during warm SSTA periods, which is consistent with the results from ERAI. These differences illustrate the dependence of GCM mean state moisture distributions on parameterized physics that lift water vapor from the ocean surface and moisten the free troposphere (Randall, 2013).

We began this study to understand how SST-modulated surface fluxes improve MJO simulation. We learned that coupling improves MJO propagation by sharpening meridional moisture gradients across the Warm Pool, thereby enhancing column moistening by meridional moisture advection east of MJO heating. In an effort to understand why coupling changes the mean-state moisture, we composited Warm Pool $-Q_2/L_v$ profiles conditioned by rainfall rate and SSTA. This yielded unexpected new insights into how parameterized convection and upper-ocean heating together influence tropical mean-state moisture patterns. This framework is potentially useful for understanding a broader array of observed phenomena, such as large-scale convective aggregation and two-way feedbacks between convection and SST perturbations on interannual-to-decadal scales. It could

also be leveraged as a process-oriented diagnostic to assess the fidelity of simulated ocean-atmosphere or land-atmosphere interactions in a hierarchy of model configurations, and to study causes of persistent model biases, such as the poor representation of tropical convectively coupled equatorial waves, SST mean-state cold biases, or the double ITCZ.

Acknowledgments

The authors are deeply indebted to Daehyun Kim, Jim Benedict, Xianan Jiang, and Paul Roundy for their thoughtful suggestions and feedback during the course of this work. Three anonymous reviewers provided constructive feedback for improving the presentation of our findings. CAD was supported by National Science Foundation (NSF) award AGS-1445191 and National Oceanic Atmospheric Administration Model Analysis, Predictions and Projections (NOAA MAPP) program award NA16OAR4310094. NPK was supported by an Independent Research Fellowship from the Natural Environment Research Council (NE/L010976/1) and NOAA MAPP award NA16OAR4310071. WLT supported by the Ministry of Science and Technology, Taiwan (MOST 107-2119-M-001-010) and performed ECHAM simulations at the National Center for High-Performance Computing. MAB was supported by the Earth System Modeling and Education Institute at Colorado State University. YG received support from the Research Innovation Program for College Graduate of Jiangsu Province (KYZZ16-0345). DAR was supported by NSF grant AGS-1538532 to Colorado State University.

References

- Adames, Á. F., Kim, D., Sobel, A. H., Del Genio, A., & Wu, J. (2017). Changes in the structure and propagation of the mjo with increasing CO₂. *Journal of Advances in Modeling Earth Systems*, 9(2), 1251–1268.
- Andersen, J. A., & Kuang, Z. (2012). Moist static energy budget of MJO-like disturbances in the atmosphere of a zonally symmetric aquaplanet. *Journal of Climate*, 25(8), 2782–2804.
- Arnold, N. P., & Randall, D. A. (2015). Global-scale convective aggregation: Implications for the Madden-Julian oscillation. *J. Adv. Model. Earth Sys.*, 7, 1499–1518. doi: 10.1002/2015MS000498
- Benedict, J. J., Maloney, E. D., Sobel, A. H., Frierson, D. M., & Donner, L. J. (2013). Tropical intraseasonal variability in version 3 of the GFDL Atmosphere

- 808 Model. *J. Climate*, *26*, 426–449.
- 809 Benedict, J. J., & Randall, D. A. (2011). Impacts of idealized air–sea coupling on
810 Madden–Julian oscillation structure in the superparameterized CAM. *J. At-*
811 *mos. Sci.*, *68*, 1990–2008.
- 812 Bernie, D. J., Woolnough, S. J., & Slingo, J. M. (2005). Modeling diurnal and in-
813 traseasonal variability of the ocean mixed layer. *J. Climate*, *18*, 1190–1202.
- 814 Bretherton, C. S., Blossey, P. N., & Khairoutdinov, M. (2005). An energy-balance
815 analysis of deep convective self-aggregation above uniform SST. *Journal of the*
816 *Atmospheric Sciences*, *62*(12), 4273–4292.
- 817 Bretherton, C. S., Peters, M. E., & Back, L. E. (2004). Relationships between water
818 vapor path and precipitation over the tropical oceans. *J. Climate*, *17*(7), 1517–
819 1528.
- 820 Chen, G., & Wang, B. (2018). Effects of enhanced front walker cell on the eastward
821 propagation of the MJO. *Journal of Climate*, *31*(19), 7719–7738. doi: 10.1175/
822 jcli-d-17-0383.1
- 823 Dee, D. P., & co authors. (2011). The ERA–Interim reanalysis: configuration and
824 performance of the data assimilation system. *Q. J. R. Meteorol. Soc.*, *137*,
825 553–597.
- 826 Del Genio, A. D., & Chen, Y. (2015). Cloud-radiative driving of the Madden-Julian
827 oscillation as seen by the A-Train. *J. Geophys. Res. Atmos.*, *120*, 5344–5356.
828 (2015JD023278) doi: 10.1002/2015JD023278
- 829 DeMott, C. A., Benedict, J. J., Klingaman, N. P., Woolnough, S. J., & Randall,
830 D. A. (2016). Diagnosing ocean feedbacks to the MJO: SST-modulated surface
831 fluxes and the moist static energy budget. *J. Geophys. Res.: Atmos.*, *121*,
832 8350–8373.
- 833 DeMott, C. A., Klingaman, N. P., & Woolnough, S. J. (2015). Atmosphere-ocean
834 coupled processes in the Madden–Julian oscillation. *Rev. Geophys.*, *53*, 1099–
835 1154. (2014RG000478)
- 836 DeMott, C. A., Randall, D. A., & Khairoutdinov, M. (2007). Convective precip-
837 itation variability as a tool for general circulation model analysis. *J. Climate*,
838 *20*(1), 91–112.
- 839 DeMott, C. A., Stan, C., Randall, D. A., & Branson, M. D. (2014). Intraseasonal
840 variability in Coupled GCMs: The roles of ocean feedbacks and model physics.

- 841 *J. Climate*, 27(13), 4970–4995.
- 842 DeMott, C. A., Wolding, B. O., Maloney, E. D., & Randall, D. A. (2018). Atmo-
 843 spheric mechanisms for MJO decay over the maritime continent. *Journal of*
 844 *Geophysical Research: Atmospheres*, 123(10), 5188–5204.
- 845 Denning, A. S., Takahashi, T., & Friedlingstein, P. (1999). KEYNOTE PER-
 846 SPECTIVE. can a strong atmospheric CO₂ rectifier effect be reconciled
 847 with a "reasonable" carbon budget? *Tellus B*, 51(2), 249–253. doi:
 848 10.1034/j.1600-0889.1999.t01-1-00010.x
- 849 de Rooy, W. C., Bechtold, P., Frhlich, K., Hohenegger, C., Jonker, H., Mironov, D.,
 850 ... Yano, J.-I. (2012). Entrainment and detrainment in cumulus convection:
 851 an overview. *Quarterly Journal of the Royal Meteorological Society*, 139(670),
 852 1–19. doi: 10.1002/qj.1959
- 853 Fu, X., Wang, W., Lee, J.-Y., Wang, B., Kikuchi, K., Xu, J., ... Weaver, S. (2015).
 854 Distinctive roles of air–sea coupling on different MJO events: A new perspec-
 855 tive revealed from the DYNAMO/CINDY field campaign. *Mon. Wea. Rev.*,
 856 143(3), 794–812.
- 857 Gao, Y., Klingaman, N. P., DeMott, C. A., & Hsu, P.-C. (2018). Diagnosing ocean
 858 feedbacks to the BSISO: SST-modulated surface fluxes and the moist static
 859 energy budget. *Journal of Geophysical Research: Atmospheres*.
- 860 Gill, A. E. (1980). Some simple solutions for heat-induced tropical circulation.
 861 *Q. J. Roy. Meteor. Soc.*, 106, 447–462.
- 862 Gonzalez, A. O., & Jiang, X. (2017). Winter mean lower tropospheric moisture over
 863 the maritime continent as a climate model diagnostic metric for the propaga-
 864 tion of the madden-julian oscillation. *Geophysical Research Letters*, 44(5),
 865 2588–2596. (2016GL072430)
- 866 Gottschalck, J., Roundy, P. E., Schreck III, C. J., Vintzileos, A., & Zhang, C.
 867 (2013). Large-scale atmospheric and oceanic conditions during the 2011–12
 868 DYNAMO field campaign. *Mon. Wea. Rev.*, 141(12), 4173–4196.
- 869 Halkides, D. J., Waliser, D. E., Lee, T., Menemenlis, D., & Guan, B. (2015). Quan-
 870 tifying the processing controlling intraseasonal mixed-layer temperature vari-
 871 ability in the tropical Indian Ocean. *J. Geophys. Res. Oceans*, 120, 692–715.
- 872 Harrison, D. E., & Vecchi, G. A. (2001). January 1999 Indian Ocean cooling event.
 873 *Geophys. Res. Lett.*, 28(19), 3717–3720.

- 874 Hirons, L. C., Klingaman, N. P., & Woolnough, S. J. (2015). MetUM-
 875 GOML: A near-globally coupled atmosphere–ocean–mixed-layer model.
 876 *Geosci. Model Dev.*, *8*, 363–379.
- 877 Hsu, P.-C., & Li, T. (2012). Role of the boundary layer moisture asymmetry in
 878 causing the eastward propagation of the Madden–Julian oscillation. *J. Cli-*
 879 *mate*, *25*, 4914–4931.
- 880 Jiang, X., Waliser, D. E., Xavier, P. K., Petch, J., Klingaman, N. P., Woolnough,
 881 S. J., ... Zhu, H. (2015). Vertical structure and physical processes of the
 882 Madden–Julian oscillation: Exploring key model physics in climate simula-
 883 tions. *J. Geophys. Res.*, *120*(10), 4718–4748.
- 884 Kawai, Y., & Wada, A. (2007). Diurnal sea surface temperature variation and
 885 its impact on the atmosphere and ocean: A review. *J. Oceanography*, *63*,
 886 721–744.
- 887 Kemball-Cook, S., Wang, B., & Fu, X. (2002). Simulation of the ISO in the
 888 ECHAM4 model: The impact of coupling with an ocean model. *J. Atmos.*
 889 *Sci.*, *59*, 1433–1453.
- 890 Kessler, W. S., & Kleeman, R. (2000). Rectification of the Madden–Julian oscillation
 891 into the ENSO cycle. *J. Climate*, *13*, 3560–3575.
- 892 Khairoutdinov, M., Randall, D., & DeMott, C. (2005). Simulations of the atmo-
 893 spheric general circulation using a cloud-resolving model as a superparameteri-
 894 zation of physical processes. *J. Atmos. Sci.*, *62*, 2136–2154.
- 895 Kim, D., Kim, H., & Lee, M.-I. (2017). Why does the MJO detour the maritime
 896 continent during austral summer? *Geophysical Research Letters*. doi: 10.1002/
 897 2017gl072643
- 898 Kim, D., Kug, J.-S., & Sobel, A. H. (2014). Propagating versus nonpropagating
 899 Madden–Julian oscillation events. *J. Climate*, *27*, 111–125.
- 900 Kim, D., Sobel, A. H., Del Genio, A. D., Chen, Y., Camargo, S. J., Yao, M.-S., ...
 901 Nazarenko, L. (2012). The tropical subseasonal variability simulated in the
 902 NASA GISS general circulation model. *J. Climate*, *25*, 4641–4659.
- 903 Kim, D., Sperber, K., Stern, W., Waliser, D., Kang, I.-S., Maloney, E., ... oth-
 904 ers (2009). Application of mjo simulation diagnostics to climate models. *J.*
 905 *Climate*, *22*(23), 6413–6436.
- 906 Kiranmayi, L., & Maloney, E. D. (2011). Intraseasonal moist static energy budget in

- reanalysis data. *Journal of Geophysical Research: Atmospheres*, 116(D21).
- Klingaman, N. P., Jiang, X., Xavier, P. K., Petch, J., Waliser, D., & Woolnough, S. J. (2015). Vertical structure and physical processes of the Madden-Julian oscillation: Synthesis and summary. *J. Geophys. Res.*, *accepted*, doi:10.1002/2015JD023196.
- Klingaman, N. P., & Woolnough, S. J. (2014). The role of air-sea coupling in the simulation of the Madden-Julian oscillation in the Hadley Centre model. *Quart. J. Roy. Meteor. Soc.*, 140, 2272–2286.
- Large, W. G., McWilliams, J. C., & Doney, S. C. (1994). Oceanic vertical mixing: A review and a model with a nonlocal boundary layer parameterization. *Rev. Geophys.*, 32(4), 363–403.
- Liebmann, B. (1996). Description of a complete (interpolated) outgoing longwave radiation dataset. *Bull. Amer. Meteor. Soc.*, 77, 1275–1277.
- Lim, Y., Son, S.-W., & Kim, D. (2018). MJO prediction skill of the subseasonal-to-seasonal prediction models. *Journal of Climate*, 31(10), 4075–4094. doi: 10.1175/jcli-d-17-0545.1
- Madden, R. A., & Julian, P. R. (1972). Description of global-scale circulation cells in the tropics with a 40–50 day period. *J. Atmos. Sci.*, 29, 1109–1123.
- Madden-Julian Oscillation Working Group, C. (2009). MJO simulation diagnostics. *J. Climate*, 22, 3006–3030.
- Madec, G. (2008). *Nemo ocean engine*. Note du Pôle de modélisation, Institut Pierre-Simon Laplace (IPSL), France, No 27, ISSN No 1288-1619.
- Maloney, E. D. (2009). The moist static energy budget of a composite tropical intraseasonal oscillation in a climate model. *J. Climate*, 22, 711–729.
- Maloney, E. D., & Sobel, A. H. (2004). Surface fluxes and ocean coupling in the tropical intraseasonal oscillation. *J. Climate*, 17, 4368–4386.
- Marshall, A. G., Alves, O., & Hendon, H. H. (2008). An enhanced moisture convergence–evaporation mechanism for MJO air-sea interaction. *J. Atmos. Sci.*, 65, 970–986.
- McPhaden, M. J., & Foltz, G. R. (2013). Intraseasonal variations in the surface layer heat balance of the central equatorial Indian Ocean: The importance of zonal advection and vertical mixing. *Geophys. Res. Lett.*, 40(11), 2737–2741. Retrieved from <http://dx.doi.org/10.1002/grl.50536> doi:

- 10.1002/grl.50536
- Moum, J. N., de Szoeke, S. P., Smyth, W. D., Edson, J. B., DeWitt, H. L., Moulin, A. J., ... et al. (2013). Air-sea interactions from westerly wind bursts during the November 2011 MJO in the Indian Ocean. *Bull. Amer. Meteor. Soc.*, 140110130153004.
- Moum, J. N., Pujiana, K., Lien, R.-C., & Smyth, W. D. (2016). Ocean feedback to pulses of the Madden-Julian oscillation in the equatorial Indian Ocean. *Nature communications*, 7.
- Neelin, J. D., Held, I. M., & Cook, K. H. (1987). Evaporation-wind feedback and low-frequency variability in the tropical atmosphere. *J. Atmos. Sci.*, 44, 2341–2348.
- Neelin, J. D., Peters, O., & Hales, K. (2009). The transition to strong convection. *Journal of the Atmospheric Sciences*, 66(8), 2367–2384. Retrieved from <https://doi.org/10.1175%2F2009jas2962.1> doi: 10.1175/2009jas2962.1
- Neena, J., Lee, J. Y., Waliser, D., Wang, B., & Jiang, X. (2014). Predictability of the madden-julian oscillation in the intraseasonal variability hindcast experiment (isvhe)*. *J. Climate*, 27(12), 4531–4543.
- Pegion, K., & Kirtman, B.-P. (2008). The impact of air-sea interactions on the predictability of the tropical intraseasonal oscillation. *J. Climate*, 21, 5870–5886.
- Pohl, B., & Matthews, A. J. (2007). Observed changes in the lifetime and amplitude of the Madden-Julian oscillation associated with interannual ENSO sea surface temperature anomalies. *J. Climate*, 20, 2659–2674.
- Randall, D. A. (2013). Beyond deadlock. *Geophysical Research Letters*, 40(22), 5970–5976. doi: 10.1002/2013gl057998
- Riley Dellaripa, E., & Maloney, E. D. (2015). Analysis of MJO wind-flux feedbacks in the Indian Ocean using RAMA observations. *J. Meteorol. Soc. Jpn.*, 93(0), 1–20.
- Saji, N. H., Xie, S.-P., & Tam, C.-Y. (2006). Satellite observations of intense intraseasonal cooling events in the tropical south Indian Ocean. *Geophys. Res. Lett.*, 33, L14704.
- Seiki, A., Katsumata, M., Horii, T., Hasegawa, T., Richards, K. J., Yoneyama, K., & Shirooka, R. (2013). Abrupt cooling associated with the oceanic Rossby wave and lateral advection during CINDY2011. *J. Geophys. Res. Oceans*, 118,

- 5523-5535.
- Seo, K.-H., Schemm, J.-K. E., Wang, W., & Kumar, A. (2007). The boreal summer intraseasonal oscillation simulations in the NCEP Climate Forecast System: The effect of sea surface temperature. *Mon. Wea. Rev.*, *135*, 1807–1827.
- Shinoda, T. (2005). Impact of diurnal cycle of solar radiation on intraseasonal SST variability in the western equatorial Pacific. *J. Climate*, *18*, 2628–2636.
- Shinoda, T., & Hendon, H. H. (2002). Rectified wind forcing and latent heat flux produced by the madden–julian oscillation. *Journal of Climate*, *15*(23), 3500–3508. doi: 10.1175/1520-0442(2002)015<3500:rwfalh>2.0.co;2
- Slingo, J. M., & co authors. (1996). Intraseasonal oscillations in 15 atmospheric general circulation models: Results from an amip diagnostics subproject. *Clim. Dynam.*, *12*(325-357).
- Smith, R. D., & Gent, P. (2002). (Tech. Rep. No. LA-UR-02-2484). Los Alamos National Laboratory.
- Sperber, K. R., Gualdi, S., Legutke, S., & Gayler, V. (2005). The Madden–Julian oscillation in ECHAM4 coupled and uncoupled general circulation models. *Clim. Dynam.*, *25*, 117–140.
- Stan, C., Khairoutdinov, M., DeMott, C. A., Krishnamurthy, V., Straus, D. M., Randall, D. A., ... Shukla, J. (2010). An ocean-atmosphere climate simulation with an embedded cloud resolving model. *Geophys. Res. Lett.*, *37*, L01702.
- Stevens, B., Giorgetta, M., Esch, M., Mauritsen, T., Crueger, T., Rast, S., ... Roeckner, E. (2013). Atmospheric component of the MPI-m earth system model: ECHAM6. *Journal of Advances in Modeling Earth Systems*, *5*(2), 146–172. doi: 10.1002/jame.20015
- Thayer-Calder, K., & Randall, D. A. (2009). The role of convective moistening in the Madden-Julian oscillation. *J. Atmos. Sci.*, *66*, 3297–3312.
- Tseng, W.-L., Tsuang, B.-J., Keenlyside, N. S., Hsu, H.-H., & Tu, C.-Y. (2015). Resolving the upper–ocean warm layer improves the simulation of the Madden–Julian oscillation. *Clim. Dynam.*, *44*, 1487–1503.
- Voldoire, A., Sanchez-Gomez, E., y Méliá, D. S., Decharme, B., Cassou, C., Sénési, S., ... Chauvin, F. (2012). The CNRM-CM5.1 global climate model: description and basic evaluation. *Climate Dynamics*, *40*(9-10), 2091–2121. doi: 10.1007/s00382-011-1259-y

- 1006 Waliser, D. E., Lau, K. M., & Kim, J. H. (1999). The influence of coupled sea-
 1007 surface temperatures on the Madden–Julian oscillation: A model perturbation
 1008 experiment. *J. Atmos. Sci.*, *56*, 333–358.
- 1009 Walters, D. N., Best, M. J., Bushell, A. C., Copsey, D., Edwards, J. M., Falloon,
 1010 P. D., ... Williams, K. D. (2011). The Met Office Unified Model Global Atmo-
 1011 sphere 3.0/3.1 and JULES Global Land 3.0/3.1 configurations. *Geosci. Model*
 1012 *Dev.*, *4*, 919–941.
- 1013 Wang, B., Lee, S.-S., Waliser, D. E., Zhang, C., Sobel, A., Maloney, E., ... Ha, K.-
 1014 J. (2018). Dynamics-oriented diagnostics for the Madden-Julian oscillation.
 1015 *Journal of Climate*. doi: 10.1175/jcli-d-17-0332.1
- 1016 Wang, B., & Xie, X. (1998). Coupled modes of the warm pool climate system. Part
 1017 I: The role of air-sea interaction in maintaining Madden–Julian oscillations.
 1018 *J. Climate*, *8*, 2116–2135.
- 1019 Wang, L., Li, T., Maloney, E., & Wang, B. (2017). Fundamental causes of propagat-
 1020 ing and nonpropagating MJOs in MJOTF/GASS models. *Journal of Climate*,
 1021 *30*(10), 3743–3769. doi: 10.1175/jcli-d-16-0765.1
- 1022 Wang, W., & Seo, K.-H. (2009). The Madden–Julian oscillation in NCEP coupled
 1023 model simulation. *Terr. Atmos. Ocean. Sci.*, *20*, 713–725.
- 1024 Watterson, I. G. (2002). The sensitivity of subannual and intraseasonal tropical vari-
 1025 ability to model ocean mixed layer depth. *J. Geophys. Res.*, *107*, D24020.
- 1026 Wheeler, M. C., & Hendon, H. H. (2004). An all-season real-time multivariate MJO
 1027 index: Development and index for monitoring and prediction. *Mon. Wea. Rev.*,
 1028 *132*, 1917–1932.
- 1029 Williams, E. R. (1994). Global circuit response to seasonal variations in global sur-
 1030 face air temperature. *Monthly Weather Review*, *122*(8), 1917–1929.
- 1031 Yanai, M., Esbensen, S., & Chu, J.-H. (1973). Determination of bulk properties
 1032 of tropical cloud clusters from large-scale heat and moisture budgets. *J. At-*
 1033 *mos. Sci.*, *30*, 611–627.
- 1034 Yang, D. (2018). Boundary layer diabatic processes, the virtual effect, and convec-
 1035 tive self-aggregation. *Journal of Advances in Modeling Earth Systems*, *10*(9),
 1036 2163–2176.
- 1037 Yokoi, S., Katsumata, M., & Yoneyama, K. (2014). Variability in surface meteo-
 1038 rology and air-sea fluxes due to cumulus convective systems observed during

- 1039 CINDY/DYNAMO. *J. Geophys. Res. Atmos.*, *119*, 2064-2078.
- 1040 Zhang, C., Dong, M., Gualdi, S., Hendon, H. H., Maloney, E. D., Marshall, A., ...
- 1041 Wang, W. (2006). Simulations of the Madden–Julian oscillation in four pairs
- 1042 of coupled and uncoupled global models. *Clim. Dyn.*, *27*, 573–592.
- 1043 Zhang, C., & McPhaden, M. J. (2000). Intraseasonal surface cooling in the equato-
- 1044 rial western Pacific. *J. Climate*, *13*, 2261–2276.